Oden Institute REPORT 20-08

May 2020

Mixed stress-displacement isogeometric collocation for nearly incompressible elasticity and elastoplasticity

by

Frederik Fahrendorf, Simone Morganti, Alessandro Reali, Thomas J.R. Hughes, and Laura De Lorenzis

Oden Institute for Computational Engineering and Sciences
The University of Texas at Austin
Austin, Texas 78712

Reference: Frederik Fahrendorf, Simone Morganti, Alessandro Reali, Thomas J.R. Hughes, and Laura De Lorenzis, "Mixed stress-displacement isogeometric collocation for nearly incompressible elasticity and elastoplasticity," Oden Institute REPORT 20-08, Oden Institute for Computational Engineering and Sciences, The University of Texas at Austin, May 2020.

Mixed stress-displacement isogeometric collocation for nearly incompressible elasticity and elastoplasticity

Frederik Fahrendorf[a,*], Simone Morganti[b], Alessandro Reali[c], Thomas J.R. Hughes[d], Laura De Lorenzis[a]

[a] *Institute of Applied Mechanics, Technische Universität Braunschweig, Pockelsstraße 3, 38106 Braunschweig, Germany*
[b] *Department of Electrical, Computer, and Biomedical Engineering, University of Pavia, Via Ferrata 5, 27100 Pavia, Italy*
[c] *Department of Civil Engineering and Architecture, University of Pavia, Via Ferrata 3, 27100 Pavia, Italy*
[d] *Institute for Computational Engineering and Sciences (ICES), University of Texas at Austin, 201 East 24th Street, Austin, TX 78712, USA*

Abstract

We propose a mixed stress-displacement isogeometric collocation method for nearly incompressible elastic materials and for materials exhibiting von Mises plasticity. The discretization is based on isogeometric analysis (IGA) with non-uniform rational B-Splines (NURBS) as basis functions. As compared to conventional IGA Galerkin formulations, isogeometric collocation methods offer a high potential of computational cost reduction for higher-order discretizations as they eliminate the need for quadrature. In the proposed mixed formulation, both stress and displacement fields are approximated as primary variables with the aim of treating volumetric locking and instability issues, which occur in displacement-based isogeometric collocation for nearly incompressible elasticity and von Mises plasticity. The performance of the proposed approach is demonstrated by several numerical examples.

Keywords: Isogeometric Analysis, Isogeometric Collocation, Volumetric Locking, Elastoplasticity, Mixed Stress-Displacement Formulation.

1. Introduction

Isogeometric Analysis (IGA) can be considered as an extension of the finite element method (FEM), with which it shares many characteristics. In contrast to the classical FEM, discretizations in the IGA framework make use of smooth and higher-order basis functions, which are popular in Computer Aided Design (CAD) environments, such as B-Splines or non-uniform rational B-Splines (NURBS).

The main original purpose of its proposers [1, 2] was to realize a seamless interaction of design and analysis. Since the introduction in [1, 2], it became clear that apart from the original motivation, the higher accuracy per degree of freedom (DOF) makes IGA appealing

*Corresponding author.
Email address: `f.fahrendorf@tu-braunschweig.de` (Frederik Fahrendorf)

for many applications. Nevertheless, the issue of computational efficiency arises, mainly due to the cost of quadrature. Standard Gaussian quadrature rules are not well-suited for IGA, since they do not exploit the higher continuity of isogeometric basis functions. This leads to a large computational effort for the assembly of IGA system matrices, especially when basis functions of high polynomial degree are used.

In the past years, many different approaches regarding alternative quadrature rules have been proposed, striving at a reduction of the computational cost as, e.g., presented in [3, 4, 5, 6, 7, 8, 9, 10, 11]. Moreover, parallel implementations on GPUs [12] or other strategies to accelerate IGA computations as for instance in [13, 14, 15, 16] have also been proposed.

Besides the aforementioned approaches, which are mainly based on Galerkin formulations, isogeometric collocation methods have recently been proposed with the goal of achieving further computational cost reduction. In isogeometric collocation methods, the strong form of the governing differential equations is directly enforced at a set of evaluation points, thus there is no need for numerical quadrature of integral equations, which is often computationally expensive. Isogeometric collocation approaches have been successfully applied to various problems of solid and structural mechanics, such as shown for example in [17, 18, 19, 20, 21, 22, 23, 24, 25, 26, 27]. Further improvements of their efficiency could be obtained by the application of the superconvergence theory to the isogeometric collocation concept as demonstrated, e.g., in [28, 29, 30, 31] and by bridging the gap between collocation and Galerkin methods [29, 32]. Thus far, most of the studies regarding isogeometric collocation have been concerned with linear or smooth non-linear problems. For non-linear problems, the demand for computationally efficient numerical methods is significant, due to the need for an iterative solution procedure and, in many cases, for a fine resolution of the spatial discretization.

In this work, we address elastoplastic material behaviour, adopting classical von Mises plasticity in conjunction with the standard return-mapping algorithm for time integration (see, e.g., [33, 34, 35, 36, 37]). The non-smoothness inherent to the transition between elastic and plastic behaviour raises stability issues for displacement-based collocation methods. Moreover, since the plastic flow in the considered plasticity model is isochoric, issues of volumetric locking can be envisioned for the primal formulation. Therefore, the topic of volumetric locking is investigated decidedly before the elastoplastic material behaviour is considered, namely for the case of nearly incompressible elasticity. There exists a broad variety of strategies against volumetric locking, which have been already applied to IGA Galerkin, such as (selective) reduced integration [6], enhanced assumed strain [38], B-bar and F-bar methods [39, 40] and mixed formulations [41, 42, 43].

In this contribution, we propose a mixed formulation where both stress and displacement fields are approximated as primary variables. The objective is twofold. On one hand, we aim at addressing volumetric locking issues, which we investigate for nearly incompressible elastic materials. On the other hand, we intend to solve the stability concerns of the primal collocation formulation for elastoplasticity, where the mixed approach also takes care of the volumetric incompressibility arising from the von Mises model. To the best of the authors knowledge, this paper reports the first attempt to combine a mixed stress-displacement approach with isogeometric collocation for solid mechanics. In the companion paper [44] a displacement-pressure formulation for isogeometric collocation is instead proposed. Examples of a mixed stress-displacement approach applied to elastoplasticity in a FEM environment can, e.g., be found in [45, 46]. A mixed stress-displacement isogeometric formulation for the analysis of elastoplastic solid-shell elements is reported in [47] and mixed isogeometric collocation methods are investigated in [48, 49, 50, 51, 52, 53].

Since CAD geometries in engineering practice usually consist of multiple patches, suitable coupling strategies are necessary. In this realm, it is shown how the proposed approach can be extended to multi-patch parameterizations. In the IGA Galerkin framework various multi-patch coupling strategies have been proposed, see, e.g., [54, 55, 56, 57, 58, 59], which usually deal with non-conforming multi-patch parameterizations. In the present context of mixed isogeometric collocation methods, we consider conforming multi-patch geometries for the sake of simplicity. A comparable approach for a primal isogeometric collocation method can be found in [18].

This paper is organized as follows: In section 2 the governing solid mechanics equations are given and the time discretization is addressed. In section 3 the considered spatial discretizations are highlighted and the proposed mixed stress-displacement approach is illustrated. Also the extension to multi-patch parameterizations and a hybrid collocation-Galerkin approach are described. Several numerical examples featuring nearly incompressible material elastic behaviour are investigated in section 4, while the results obtained with the elastoplastic material model are illustrated in section 5. Conclusions are drawn and future research directions are outlined in section 6.

2. Governing equations and return mapping algorithm

In this section, the governing equations for the solid mechanics problem and the time integration algorithm needed for elastoplasticity are described. Firstly, the case of linear elastic materials at small strains is addressed. Subsequently, the extension to von Mises plasticity with isotropic hardening is considered. The return-mapping algorithm, applied for the time integration of the elastoplastic constitutive equations, is also outlined. Although plane strain conditions are used to model the numerical examples in sections 4 and 5, the more general three-dimensional case is considered for the derivations, since the plane strain condition can be simply incorporated afterwards.

2.1. Balance and kinematic equations and boundary conditions

This work considers quasi-static linear elastic and elastoplastic problems. The governing equations include balance, kinematic and constitutive equations, along with boundary conditions. The balance of momentum localized at any point of a body within the domain $\Omega \subset \mathbb{R}^d$ (with d as the spatial dimension) reads

$$\nabla \cdot \boldsymbol{\sigma} + \boldsymbol{b} = \boldsymbol{0} \qquad \text{in } \Omega. \tag{1}$$

Here $\nabla\cdot$ is the divergence operator, $\boldsymbol{\sigma}$ is the stress tensor and $\boldsymbol{b}$ is the body force vector. The momentum balance is complemented by the boundary conditions

$$\boldsymbol{\sigma} \cdot \boldsymbol{n} = \boldsymbol{t} \qquad \text{on } \Gamma_N, \tag{2a}$$

$$\boldsymbol{u} = \bar{\boldsymbol{u}} \qquad \text{on } \Gamma_D, \tag{2b}$$

where $\boldsymbol{t}$ is the prescribed traction on the Neumann boundary Γ_N, $\boldsymbol{n}$ is the outward unit normal to the boundary Γ, $\boldsymbol{u}$ is the vector of the unknown displacements and $\bar{\boldsymbol{u}}$ are the imposed displacements on the Dirichlet boundary Γ_D, with $\Gamma = \Gamma_N \cup \Gamma_D$ and $\Gamma_N \cap \Gamma_D = \emptyset$.

In case of small deformations, the strain tensor is defined as

$$\boldsymbol{\varepsilon} = \nabla^S \boldsymbol{u} = \frac{1}{2}(\nabla \boldsymbol{u} + (\nabla \boldsymbol{u})^T), \tag{3}$$

where ∇ is the gradient operator and ∇^S denotes the symmetric gradient operator.

2.2. Constitutive material models

In this subsection the constitutive material models, which relate the strain tensor $\boldsymbol{\varepsilon}$ with the stress tensor $\boldsymbol{\sigma}$, are described. Material models for linear elasticity and elastoplasticity are considered in this work.

2.2.1. Linear elasticity

Under the assumption of linearly elastic isotropic material behaviour, the stress tensor $\boldsymbol{\sigma}$ and the strain tensor $\boldsymbol{\varepsilon}$ are related by the following constitutive equation

$$\boldsymbol{\sigma} = \mathbb{C} : \boldsymbol{\varepsilon} \tag{4}$$

with the fourth-order elasticity tensor $\mathbb{C}$ defined as

$$\mathbb{C} = \lambda \mathbf{1} \otimes \mathbf{1} + 2\mu \mathbf{I} = \kappa \mathbf{1} \otimes \mathbf{1} + 2\mu \left(\mathbf{I} - \frac{1}{3} \mathbf{1} \otimes \mathbf{1} \right), \tag{5}$$

where $\mathbf{1} = \delta_{ij} \mathbf{e}_i \otimes \mathbf{e}_j$ is the second-order identity tensor, $\mathbf{I} = \frac{1}{2}\left[\delta_{ik}\delta_{jl} + \delta_{il}\delta_{jk}\right] \mathbf{e}_i \otimes \mathbf{e}_j \otimes \mathbf{e}_k \otimes \mathbf{e}_l$ is the fourth-order symmetric identity tensor, λ, μ are the Lamé constants and $\kappa = \lambda + \frac{2}{3}\mu$ is the bulk modulus.

If nearly incompressible materials are modeled, the first Lamé constant λ becomes very large. This might lead to an overly stiff behaviour and even loss of spatial convergence in the solution of the discretized problem, which is known as volumetric locking. In this work a mixed method is introduced to mitigate the effect of volumetric locking.

2.2.2. Elastoplasticity

If an elastoplastic material model with small deformations is considered, the total strain tensor $\boldsymbol{\varepsilon}$ can be additively decomposed as $\boldsymbol{\varepsilon} = \boldsymbol{\varepsilon}^e + \boldsymbol{\varepsilon}^p$ into the elastic strain tensor $\boldsymbol{\varepsilon}^e$ and the plastic strain tensor $\boldsymbol{\varepsilon}^p$. Then the stress tensor $\boldsymbol{\sigma}$ can be calculated as $\boldsymbol{\sigma} = \mathbb{C} : (\boldsymbol{\varepsilon} - \boldsymbol{\varepsilon}^p)$.

In this work the classical von Mises plasticity with linear isotropic hardening (see, e.g., [33, 34]) is adopted. The yield condition reads

$$f(\boldsymbol{\sigma}, \alpha) = \|\mathbf{s}\| - \sqrt{\frac{2}{3}}[\sigma_Y + K\alpha] \leq 0 \tag{6}$$

with the deviatoric stress tensor $\mathbf{s} = \operatorname{dev}[\boldsymbol{\sigma}] = \boldsymbol{\sigma} - \frac{1}{3}\operatorname{tr}[\boldsymbol{\sigma}]\,\mathbf{1}$, the yield stress σ_Y, the equivalent plastic strain α and the isotropic hardening modulus K.

The evolution equations for the variables $\boldsymbol{\varepsilon}^p$ and α are given as

$$\dot{\boldsymbol{\varepsilon}}^p = \gamma \frac{\mathbf{s}}{||\mathbf{s}||}, \tag{7a}$$

$$\dot{\alpha} = \gamma \sqrt{\frac{2}{3}} \tag{7b}$$

with $\gamma \geq 0$ as the consistency parameter and a superposed dot denoting time differentiation.

Loading and unloading follow the Kuhn-Tucker complementarity conditions

$$\gamma \geq 0, \quad f(\boldsymbol{\sigma}, \alpha) \leq 0, \quad \gamma f(\boldsymbol{\sigma}, \alpha) = 0. \tag{8}$$

By enforcement of the consistency condition

$$\gamma \dot{f}(\boldsymbol{\sigma}, \alpha) = 0 \quad (\text{if } f(\boldsymbol{\sigma}, \alpha) = 0) \tag{9}$$

it is ensured that the stress path remains inside the yield surface. The consistency condition enables the determination of the consistency parameter γ. The combination with the evolution equations leads to the expression of the stress rate $\dot{\boldsymbol{\sigma}}$ in terms of the total strain rate $\dot{\boldsymbol{\varepsilon}}$ as follows

$$\dot{\boldsymbol{\sigma}} = \mathbb{C}^{ep} : \dot{\boldsymbol{\varepsilon}}, \tag{10}$$

where the continuum elastoplastic tangent modulus $\mathbb{C}^{ep}$ is defined as

$$\mathbb{C}^{ep} = \frac{\partial \boldsymbol{\sigma}}{\partial \boldsymbol{\varepsilon}} = \begin{cases} \mathbb{C} - 2\mu \frac{\mathbf{n} \otimes \mathbf{n}}{1 + \frac{K}{3\mu}} & \text{if } f = 0,\ \dot{f} = 0, \\ \mathbb{C} & \text{otherwise} \end{cases} \tag{11}$$

and

$$\mathbf{n} = \frac{\mathbf{s}}{||\mathbf{s}||}. \tag{12}$$

2.3. Return mapping algorithm

Due to the dependence of the stress on the strain history, a suitable time integration scheme is necessary for the solution of elastoplastic problems. In this work a predictor / corrector method is applied. The main concept of these methods consists of having a purely elastic prediction. If the elastic prediction is admissible, it corresponds to the sought solution. Conversely, a plastic correction step is necessary if the elastic prediction leads to a result which is outside of the yield surface and thus inadmissible.

For the plastic correction step, the classical return mapping algorithm for von Mises plasticity (see, e.g., [33, 34] for further details) is used in this contribution. The return mapping algorithm is summarized in figure 1. Here $\mathbf{e} = \operatorname{dev}[\boldsymbol{\varepsilon}] = \boldsymbol{\varepsilon} - \frac{1}{3} \operatorname{tr}[\boldsymbol{\varepsilon}] \mathbf{1}$ is the strain deviator, the superscript $(.)^{tr}$ refers to the elastic trial solution and the subscripts $(.)_{n+1}$ and $(.)_n$ refer to the current and previous time step, respectively.

1. Database at each point $\mathbf{x} \in \Omega$: $\{\mathbf{e}_n^p, \alpha_n\}$
2. Given strain field at $\mathbf{x} \in \Omega$: $\boldsymbol{\varepsilon}_{n+1} = \boldsymbol{\varepsilon}_n + \Delta\boldsymbol{\varepsilon}_n$
3. Compute elastic trial stress and test for plastic loading:

$\mathbf{e}_{n+1} = \boldsymbol{\varepsilon}_{n+1} - \frac{1}{3}\mathrm{tr}\left(\boldsymbol{\varepsilon}_{n+1}\right)\mathbf{1}$
$\mathbf{s}_{n+1}^{tr} = 2\mu\left[\mathbf{e}_{n+1} - \mathbf{e}_n^p\right]$
$\boldsymbol{\sigma}_{n+1}^{tr} = \kappa\mathrm{tr}\left(\boldsymbol{\varepsilon}_{n+1}\right)\mathbf{1} + \mathbf{s}_{n+1}^{tr}$
$f_{n+1}^{tr} = \left\|\mathbf{s}_{n+1}^{tr}\right\| - \sqrt{\frac{2}{3}}\left[\sigma_Y + K\alpha_n\right]$
if $f_{n+1}^{tr} \leq 0$ **then**
  Elastic step: Set $(.)_{n+1} = (.)_{n+1}^{tr}$ and **exit**
else
  Plastic step: Return mapping
  $\mathbf{n}_{n+1} = \frac{\mathbf{s}_{n+1}^{tr}}{\left\|\mathbf{s}_{n+1}^{tr}\right\|}$
  $\Delta\gamma = \frac{f_{n+1}^{tr}}{2\left(\mu + \frac{K}{3}\right)} > 0$
  $\boldsymbol{\sigma}_{n+1} = \kappa\mathrm{tr}\left(\boldsymbol{\varepsilon}_{n+1}\right)\mathbf{1} + \mathbf{s}_{n+1}^{tr} - 2\mu\Delta\gamma\mathbf{n}_{n+1}$
  $\mathbf{e}_{n+1}^p = \mathbf{e}_n^p + \Delta\gamma\mathbf{n}_{n+1}$
  $\alpha_{n+1} = \alpha_n + \sqrt{\frac{2}{3}}\Delta\gamma$
end

Figure 1: Return mapping algorithm for von Mises plasticity with linear isotropic hardening (cf. [33]).

In analogy to the continuum elastoplastic tangent modulus $\boldsymbol{C}^{ep}$, the so-called consistent algorithmic tangent modulus $\boldsymbol{C}_{n+1}^{alg}$ for the incremental formulation can be derived consistently with the return mapping algorithm for linear isotropic hardening as described in [33]:

$$\begin{aligned}\mathbb{C}_{n+1}^{alg} &= \frac{\partial\boldsymbol{\sigma}_{n+1}}{\partial\boldsymbol{\varepsilon}_{n+1}} \\ &= \begin{cases}\kappa\mathbf{1}\otimes\mathbf{1} + 2\mu\theta_{n+1}\left(\mathbf{I} - \frac{1}{3}\mathbf{1}\otimes\mathbf{1}\right) - 2\mu\bar{\theta}_{n+1}\mathbf{n}_{n+1}\otimes\mathbf{n}_{n+1} & f_{n+1}^{tr} > 0 \\ \mathbb{C} & f_{n+1}^{tr} \leq 0\end{cases}\end{aligned} \tag{13}$$

with

$$\theta_{n+1} = 1 - \frac{2\mu\Delta\gamma}{\left\|\mathbf{s}_{n+1}^{tr}\right\|} \tag{14}$$

and

$$\bar{\theta}_{n+1} = \frac{1}{1 + \frac{K}{3\mu}} - \left(1 - \theta_{n+1}\right). \tag{15}$$

The momentum balance equation (1) and the boundary conditions (2) read in incremental form

$$\nabla\cdot\boldsymbol{\sigma}_{n+1} + \boldsymbol{b}_{n+1} = \mathbf{0} \qquad \text{in } \Omega, \tag{16a}$$
$$\boldsymbol{\sigma}_{n+1}\cdot\boldsymbol{n} = \boldsymbol{t}_{n+1} \qquad \text{on } \Gamma_N, \tag{16b}$$
$$\boldsymbol{u}_{n+1} = \bar{\boldsymbol{u}}_{n+1} \qquad \text{on } \Gamma_D. \tag{16c}$$

3. Spatial discretization methods

This section is devoted to the description of the investigated spatial discretization methods. The discretization via NURBS, stemming from IGA, is a common feature of the Galerkin and collocation approaches. Thus, the basics on NURBS basis functions are summarized at the beginning of this section. Subsequently, the primal Galerkin formulation is introduced, followed by the description of the proposed mixed isogeometric collocation approach. This section is concluded by addressing a hybrid collocation-Galerkin approach and the extension to multi-patch parameterizations.

3.1. Basis functions

In this subsection, we review the basics of B-Spline and NURBS basis functions, which are commonly employed in modern CAD systems for design modelling. The isoparametric concept is maintained in IGA, thus both the geometry parameterization and the construction of the approximation spaces for the unknown fields are realized by the same basis functions, in this contribution NURBS.

A B-spline basis of degree p is constructed by a so-called knot vector, which is a non-decreasing sequence of real numbers

$$\boldsymbol{\Xi} = \{\xi_1, \xi_2, \dots, \xi_{n+p+1}\}, \tag{17}$$

where each ξ_i is a knot and n denotes the number of basis functions of degree p. Throughout this paper, the knot vector is assumed to be open, which implies $\xi_1 = \dots = \xi_{p+1}$ and $\xi_{n+1} = \dots = \xi_{n+p+1}$. Therefore the basis is interpolatory at both ends. If a knot has multiplicity k, the continuity of the B-spline basis is C^{p-k} at that knot. The continuity is C^∞ in the interior of a knot span.

The zeroth degree B-Spline functions $\{N_{i,0}\}_{i=1,\dots,n}$ are defined as

$$N_{i,0}(\xi) = \begin{cases} 1 & \text{if} \quad \xi_i \leq \xi < \xi_{i+1}, \\ 0 & \text{otherwise.} \end{cases} \tag{18}$$

The p-th degree B-Spline basis functions are defined by means of the Cox-de Boor recursion formula using the relation

$$N_{i,p}(\xi) = \frac{\xi - \xi_i}{\xi_{i+p} - \xi_i} N_{i,p-1}(\xi) + \frac{\xi_{i+p+1} - \xi}{\xi_{i+p+1} - \xi_{i+1}} N_{i+1,p-1}(\xi) \tag{19}$$

and adopting the convention $\frac{0}{0} = 0$.

Incorporating the so-called control points $\boldsymbol{P}_i \in \mathbb{R}^d$, a B-spline curve $\boldsymbol{C}(\xi)$ can be expressed as a linear combination of the control points $\boldsymbol{P}_i$ with the corresponding basis functions $N_{i,p}$ as

$$\boldsymbol{C}(\xi) = \sum_{i=1}^{n} N_{i,p}(\xi) \boldsymbol{P}_i. \tag{20}$$

Analogously a NURBS curve can be expressed as a linear combination of control points $\boldsymbol{P}_i$ and basis functions $R_{i,p}$ of degree p as

$$\boldsymbol{C}(\xi) = \sum_{i=1}^{n} R_{i,p}(\xi) \boldsymbol{P}_i \tag{21}$$

with

$$R_{i,p}(\xi) = \frac{w_i N_{i,p}(\xi)}{\sum_{\hat{i}=1}^{n} w_{\hat{i}} N_{\hat{i},p}(\xi)} \tag{22}$$

as the NURBS basis functions with the associated weights w_i. NURBS basis functions, such as their B-Spline progenitors, are pointwise non-negative and identical continuity characteristics apply.

Bivariate NURBS basis functions $R_{i,j}^{p,q}$ of degrees p and q in the two parametric directions ξ and η with the corresponding weights $w_{i,j}$ are defined by a product of the univariate B-spline basis functions $N_{i,p}(\xi)$, $M_{j,q}(\eta)$ as

$$R_{i,j}^{p,q}(\xi,\eta) = \frac{N_{i,p}(\xi) M_{j,q}(\eta) w_{i,j}}{\sum_{\hat{i}=1}^{n} \sum_{\hat{j}=1}^{m} N_{\hat{i},p}(\xi) M_{\hat{j},q}(\eta) w_{\hat{i},\hat{j}}}. \tag{23}$$

With the control points $\boldsymbol{P}_{i,j}$, a NURBS surface of degree p, q can thus be described as

$$\boldsymbol{S}(\xi,\eta) = \sum_{i=1}^{n} \sum_{j=1}^{m} R_{i,j}^{p,q}(\xi,\eta) \boldsymbol{P}_{i,j}. \tag{24}$$

The extension to trivariate NURBS basis functions and NURBS volumes / solids can be achieved by a completely analogue procedure and is therefore not reported. For more details the reader is referred to [60].

3.2. Displacement-based Galerkin formulation

In the following, the basics of the Galerkin formulation are outlined, since Galerkin solutions are used as reference in this work, whenever analytical solutions are not available. Elastoplastic materials are considered directly, since the treatment of linear elasticity problems can be derived as a special case.

The starting point is the time-discretized form of the momentum balance equation (along with the corresponding boundary conditions) in equation (16). The Galerkin method is based on the approximation of the corresponding weak formulation. For its definition, the following two spaces

$$\boldsymbol{\mathcal{U}}_{n+1} = \{\boldsymbol{u} | \boldsymbol{u} \in (H^1(\Omega))^d, \boldsymbol{u}|_{\Gamma_D} = \bar{\boldsymbol{u}}_{n+1}\}, \quad \boldsymbol{\mathcal{V}} = \{\boldsymbol{v} | \boldsymbol{v} \in (H^1(\Omega))^d, \boldsymbol{v}|_{\Gamma_D} = \boldsymbol{0}\} \tag{25}$$

are introduced.

The weak formulation at the current time step $n+1$ consists of finding $\boldsymbol{u}_{n+1} \in \boldsymbol{\mathcal{U}}_{\boldsymbol{n+1}}$ such that for all $\boldsymbol{v} \in \boldsymbol{\mathcal{V}}$ the non-linear equation

$$R_{n+1} = \int_{\Omega} \nabla^S \boldsymbol{v} : \boldsymbol{\sigma}_{n+1}(\boldsymbol{u}_{n+1}) d\Omega - \int_{\Omega} \boldsymbol{v} \cdot \boldsymbol{b}_{n+1} d\Omega - \int_{\Gamma_N} \boldsymbol{v} \cdot \boldsymbol{t}_{n+1} d\Gamma_N = 0 \tag{26}$$

holds.

The spatial discretization $\boldsymbol{u}^h$ of the displacement vector $\boldsymbol{u}$ is introduced as

$$\boldsymbol{u}^h = \sum_{i=1}^{n_d} R_i \hat{\boldsymbol{u}}_i \tag{27}$$

with the NURBS basis functions R_i as defined in the previous subsection 3.1, the unknown displacement control variables $\hat{\boldsymbol{u}}_i$ and n_d as the total number of unknown displacement control variables. Analogously, the approximation of the test function is introduced as

$$\boldsymbol{v}^h = \sum_{i=1}^{n_d} R_i \hat{\boldsymbol{v}}_i \tag{28}$$

with the test control variables $\hat{\boldsymbol{v}}_i$.

The spatially discretized version of equation (26) thus reads

$$R^h_{n+1} = \int_\Omega \nabla^S \boldsymbol{v}^h : \boldsymbol{\sigma}_{n+1}(\boldsymbol{u}^h_{n+1}))d\Omega - \int_\Omega \boldsymbol{v}^h \cdot \boldsymbol{b}_{n+1} d\Omega - \int_{\Gamma_N} \boldsymbol{v}^h \cdot \boldsymbol{t}_{n+1} d\Gamma_N = 0. \tag{29}$$

In this work, a Newton-Raphson scheme is applied to solve the non-linear equations on the global level. To obtain the corresponding tangent, one needs to linearize equation (29), which yields

$$\Delta R^h_{n+1} = \int_\Omega \nabla^S \boldsymbol{v}^h : \Delta\boldsymbol{\sigma}_{n+1}(\boldsymbol{u}^h_{n+1}) d\Omega \tag{30}$$

with

$$\Delta\boldsymbol{\sigma}_{n+1} = \mathbb{C}^{alg}_{n+1} : \nabla^S(\Delta \boldsymbol{u}^h_{n+1}). \tag{31}$$

Note that in this context Δ is used as a symbol to indicate the linearized increment.

3.3. Mixed stress-displacement Galerkin formulation

In order to introduce the mixed stress-displacement isogeometric collocation method, the corresponding mixed stress-displacement Galerkin formulation is presented first and the collocation approach is deduced afterwards in section 3.4. This procedure enables a straightforward introduction of a hybrid collocation-Galerkin approach in section 3.5.

For the mixed stress-displacement formulation, the stress is introduced in form of the additional variable $\tilde{\boldsymbol{\sigma}}$. In the context of the Galerkin method, the equality between the newly introduced stress tensor $\tilde{\boldsymbol{\sigma}}$ and the stress tensor $\boldsymbol{\sigma}$ calculated from the displacement vector $\boldsymbol{u}$ is weakly enforced over the whole domain.

First the additional space

$$\boldsymbol{\mathcal{S}} = \{\tilde{\boldsymbol{\sigma}} | \tilde{\boldsymbol{\sigma}} \in (L^2(\Omega))^{d\times d}\} \tag{32}$$

is defined. The mixed form of the weak formulation at the current time step $n+1$ consists of finding $\boldsymbol{u}_{n+1} \in \boldsymbol{\mathcal{U}}_{n+1}$ and $\tilde{\boldsymbol{\sigma}}_{n+1} \in \boldsymbol{\mathcal{S}}$ such that for all $\boldsymbol{v} \in \boldsymbol{\mathcal{V}}$ and $\boldsymbol{w} \in \boldsymbol{\mathcal{S}}$ the weak momentum balance equation (including boundary conditions)

$$R^{mom}_{n+1} = \int_\Omega \nabla^S \boldsymbol{v} : \tilde{\boldsymbol{\sigma}}_{n+1} d\Omega - \int_\Omega \boldsymbol{v} \cdot \boldsymbol{b}_{n+1} d\Omega - \int_{\Gamma_N} \boldsymbol{v} \cdot \boldsymbol{t}_{n+1} d\Gamma_N = 0 \tag{33}$$

and the weak stress coupling equation

$$R^{str}_{n+1} = \int_\Omega \boldsymbol{w} : (\tilde{\boldsymbol{\sigma}}_{n+1} - \boldsymbol{\sigma}_{n+1}(\boldsymbol{u}_{n+1}))d\Omega = 0 \tag{34}$$

are fulfilled.

The spatial discretization $\tilde{\boldsymbol{\sigma}}^h$ of the newly introduced stress tensor $\tilde{\boldsymbol{\sigma}}$ is given as

$$\tilde{\boldsymbol{\sigma}}^h = \sum_{i=1}^{n_s} R_i \hat{\boldsymbol{\sigma}}_i \tag{35}$$

with the NURBS basis functions R_i, the unknown stress control variables $\hat{\boldsymbol{\sigma}}_i$ and n_s as the total number of stress control variables. Analogously, the approximation of the corresponding test functions is defined as

$$\boldsymbol{w}^h = \sum_{i=1}^{n_s} R_i \hat{\boldsymbol{w}}_i. \tag{36}$$

Note that the shear components σ_{xy} and σ_{yx} are discretized as a single DOF and not independently in order to reduce the number of DOFs and to enforce the symmetry of the stress tensor.

The spatially discretized versions of equations (33) and (34) read

$$R_{n+1}^{mom,h} = \int_\Omega \nabla^S \boldsymbol{v}^h : \tilde{\boldsymbol{\sigma}}_{n+1}^h d\Omega - \int_\Omega \boldsymbol{v}^h \cdot \boldsymbol{b}_{n+1} d\Omega - \int_{\Gamma_N} \boldsymbol{v}^h \cdot \boldsymbol{t}_{n+1} d\Gamma_N = 0, \tag{37}$$

$$R_{n+1}^{str,h} = \int_\Omega \boldsymbol{w}^h : (\tilde{\boldsymbol{\sigma}}_{n+1}^h - \boldsymbol{\sigma}_{n+1}(\boldsymbol{u}_{n+1}^h)) d\Omega = 0. \tag{38}$$

The linearizations of equations (37) and (38) are given in the discretized version as

$$\Delta R_{n+1}^{mom,h} = \int_\Omega \nabla^S \boldsymbol{v}^h : \Delta \tilde{\boldsymbol{\sigma}}_{n+1}^h d\Omega \tag{39}$$

and

$$\Delta R_{n+1}^{str,h} = \int_\Omega \boldsymbol{w}^h : (\Delta \tilde{\boldsymbol{\sigma}}_{n+1}^h - \Delta \boldsymbol{\sigma}_{n+1}(\boldsymbol{u}_{n+1}^h)) d\Omega, \tag{40}$$

respectively, where $\Delta \boldsymbol{\sigma}_{n+1}(\boldsymbol{u}_{n+1}^h)$ can be calculated as shown in equation (31).

3.4. Mixed stress-displacement isogeometric collocation formulation

In contrast to weighted residual formulations, the concept of isogeometric collocation is based on the direct evaluation of the strong form of the boundary value problem. In this work, a mixed approach is considered, where both stresses and displacements are independently discretized.

To deduce the proposed isogeometric collocation approach from the mixed Galerkin method, the weak momentum balance equation (33) is integrated by parts such that there are no more derivatives on the test functions:

$$R_{n+1}^{mom} = -\int_\Omega \boldsymbol{v} \cdot (\nabla \cdot \tilde{\boldsymbol{\sigma}}_{n+1} + \boldsymbol{b}_{n+1}) d\Omega + \int_{\Gamma_N} \boldsymbol{v} \cdot (\tilde{\boldsymbol{\sigma}}_{n+1} \cdot \boldsymbol{n} - \boldsymbol{t}_{n+1}) d\Gamma_N = 0. \tag{41}$$

Note that this increases the demand on the regularity of $\tilde{\boldsymbol{\sigma}}_{n+1}$, which must now belong to the Hilbert space $\boldsymbol{H}(div, \Omega)$.

In the Galerkin approaches described before, NURBS are used for the discretization of the test functions, as shown in equations (28) and (36). For the isogeometric collocation approach Dirac delta functions δ are chosen as test functions. These functions satisfy the so-called sifting property, i.e.,

$$\int_{\Omega} f_{\Omega}(\boldsymbol{\tau})\delta(\boldsymbol{\tau}-\boldsymbol{\tau}_{ij})d\Omega = f_{\Omega}(\boldsymbol{\tau}_{ij}), \tag{42}$$

$$\int_{\Gamma} f_{\Gamma}(\boldsymbol{\tau})\delta(\boldsymbol{\tau}-\boldsymbol{\tau}_{ij})d\Gamma = f_{\Gamma}(\boldsymbol{\tau}_{ij}) \tag{43}$$

for every function f_{Ω} continuous about the point $\boldsymbol{\tau}_{ij} \in \Omega$ and for every function f_{Γ} continuous about the point $\boldsymbol{\tau}_{ij} \in \Gamma$ [21, 17, 18].

By applying the sifting property to equations (41) and (34) it can be deduced that the following strong form equations, expressed in terms of displacements and stresses as independent variables, have to be solved at the set of collocation points $\boldsymbol{\tau}^{u}_{ij}$ and $\boldsymbol{\tau}^{\sigma}_{ij}$:

$$[\nabla \cdot \tilde{\boldsymbol{\sigma}}_{n+1} + \boldsymbol{b}_{n+1}](\boldsymbol{\tau}^{u}_{ij}) = \mathbf{0} \qquad \boldsymbol{\tau}^{u}_{ij} \in \Omega, \tag{44a}$$

$$[\tilde{\boldsymbol{\sigma}}_{n+1} - \boldsymbol{\sigma}_{n+1}(\boldsymbol{u}_{n+1})](\boldsymbol{\tau}^{\sigma}_{ij}) = \mathbf{0} \qquad \boldsymbol{\tau}^{\sigma}_{ij} \in \Omega, \tag{44b}$$

$$[\tilde{\boldsymbol{\sigma}}_{n+1} \cdot \boldsymbol{n} - \boldsymbol{t}_{n+1}](\boldsymbol{\tau}^{u}_{ij}) = \mathbf{0} \qquad \boldsymbol{\tau}^{u}_{ij} \in \Gamma_N. \tag{44c}$$

The set of collocation points $\boldsymbol{\tau}^{u}_{ij}$ and $\boldsymbol{\tau}^{\sigma}_{ij}$ is obtained from to the discretization of the displacement and stress fields, respectively. A common choice for the collocation point locations in the IGA framework are the images of the Greville abscissae, which can be calculated for a one-dimensional B-Spline of degree p as

$$\hat{\tau}_i = \frac{1}{p}\sum_{j=i+1}^{i+p} \xi_j, \tag{45}$$

where ξ_j are the entries of the knot vector $\boldsymbol{\Xi}$. For multi-variate discretizations, the Greville abscissae are obtained via the tensor product of equation (45) in the corresponding parametric directions. As mentioned in the introduction, there exist more advanced strategies to find improved abscissae values as e.g. shown in [28, 29, 30, 31]. However these approaches are not directly applicable to mixed formulations, especially in case of non-linear problems, hence they are not adopted herein.

For the trial functions $\boldsymbol{u}^h_{n+1}$ and $\tilde{\boldsymbol{\sigma}}^h_{n+1}$ the same discretizations with NURBS as in the mixed Galerkin method (see equations (27) and (35)) are used for the collocation method. Thus the discretized equations in residual form read

$$\boldsymbol{R}^{mom,h}_{n+1} = \nabla \cdot \tilde{\boldsymbol{\sigma}}^h_{n+1} + \boldsymbol{b}_{n+1} = \mathbf{0}, \tag{46}$$

$$\boldsymbol{R}^{str,h}_{n+1} = \tilde{\boldsymbol{\sigma}}^h_{n+1} - \boldsymbol{\sigma}_{n+1}(\boldsymbol{u}^h_{n+1}) = \mathbf{0}, \tag{47}$$

$$\boldsymbol{R}^{neu,h}_{n+1} = \tilde{\boldsymbol{\sigma}}^h_{n+1} \cdot \boldsymbol{n} - \boldsymbol{t}_{n+1} = \mathbf{0}. \tag{48}$$

The corresponding linearizations are easily obtained as

$$\Delta\boldsymbol{R}^{mom,h}_{n+1} = \nabla \cdot \Delta\tilde{\boldsymbol{\sigma}}^h_{n+1}, \tag{49}$$

$$\Delta \boldsymbol{R}_{n+1}^{str,h} = \Delta \tilde{\boldsymbol{\sigma}}_{n+1}^{h} - \Delta \boldsymbol{\sigma}_{n+1}(\boldsymbol{u}_{n+1}^{h}), \tag{50}$$

$$\Delta \boldsymbol{R}_{n+1}^{neu,h} = \Delta \tilde{\boldsymbol{\sigma}}_{n+1}^{h} \cdot \boldsymbol{n}. \tag{51}$$

The same linearization of the stress tensor $\Delta\boldsymbol{\sigma}_{n+1}(\boldsymbol{u}_{n+1})$ as given in equation (31) for the Galerkin method is also valid for the proposed mixed collocation method. Therefore, the same source code at the material point level can be used to incorporate the constitutive equations. In contrast to a pure displacement-based collocation approach, it is not necessary to linearise the algorithmic tangent modulus of the return mapping algorithm in the proposed method. Therefore, instabilities due to the non-differentiability of the tangent modulus at the elastoplastic boundary are circumvented.

3.5. Hybrid approach

The treatment of the boundary regions plays an important role in isogeometric collocation methods. In [18] the influence of the definition of normals at corner points has been studied in detail. Further investigations on the treatment of Neumann boundary conditions have been conducted in [22]. In the latter study it is shown that the strong imposition of Neumann boundary conditions may lead to a significant loss in accuracy induced by spurious oscillations. In this context two strategies were proposed. The first one is called "enhanced collocation", whereby the Neumann boundary conditions are imposed considering both boundary and bulk contributions weighted through a penalty-like constant. The second approach is named "hybrid collocation" and is characterised by the evaluation of the boundary contributions in an integral form. For more details the reader is referred to [22].

Based on this hybrid formulation, an adaptive hybrid approach for isogeometric collocation has been introduced and applied to phase-field fracture models in [61]. It is shown in section 3.4 that the mixed isogeometric collocation method can be derived from the mixed isogeometric Galerkin formulation by using Dirac delta functions as test functions. This can also be done selectively for each NURBS basis function, enabling a local switch between the Galerkin and the collocation method.

To avoid issues induced by the boundaries in the linear elastic examples of this work and still maintaining an efficient approach, only the test functions corresponding to boundary control points are kept as NURBS in the momentum balance equation, whereas the other ones are discretized by Dirac delta functions. To enable a comparison between the hybrid and the standard approach, the results of the collocation approach without hybrid treatment of the boundaries are reported in the appendix.

For the examples on elastoplasticity, the test functions of the momentum balance equation are all approximated by NURBS. Since the corresponding system of equations has to be initialized only once at the beginning of the simulation and remains the same over all load steps and Newton-Raphson iterations, the additional effort is comparatively low.

3.6. Multi-patch parameterizations

A multi-patch parameterization of a geometry is taken into account in this study, since complex geometries of real simulation models usually consist of several patches. A domain $\Omega \subset \mathbb{R}^d$, composed of N non-overlapping domains Ω^i such that $\Omega = \Omega^1 \cup \Omega^2 \cup ... \cup \Omega^N$, is considered. The coupling interface $\Gamma_{j,k}^c$ between two adjacent patches can thus be determined as $\Gamma_{j,k}^c = \Omega^j \cap \Omega^k$.

In this study, a conforming multi-patch configuration is tested, which means that the parameterizations of adjacent boundaries exactly match. Thus, in case of NURBS, the degree and the knot vectors at connected interfaces have to be identical. The patch interfaces can be coupled via linear constraints on the corresponding boundary control points. In the case of the proposed mixed isogeometric collocation approach, one needs to decide which DOFs should be coupled at the boundaries of the multi-patch parameterizations. In this work, the displacement DOFs are coupled between adjacent patches. An additional coupling of the stress DOFs led in some cases to a negative effect on the convergence of the Newton-Raphson method and is therefore omitted. Thus the continuity of the stress field is not enforced in the formulation. Kapl et. al [62] recently presented a multi-patch approach for isogeometric collocation, which leads to a globally C^2-smooth discretization space. An extension of this approach to the mixed formulation presented in this manuscript might be an interesting field of research for further studies. The coupling of the displacement DOFs is enforced strongly via the control points. Similarly, the Galerkin formulation was extended to conforming multi-patch parameterizations in order to have an equivalent reference solution.

4. Numerical examples on nearly incompressible elasticity

In this section, the behaviour of the proposed approach regarding volumetric locking effects in case of nearly incompressible elastic material behaviour is studied by means of three examples. Since the choice of the approximation spaces can have a significant influence on the locking behaviour, different combinations are compared with each other. In a Galerkin framework the corresponding mixed formulation leads to a saddle-point problem and the inf-sup condition can be used as a criterion to select suitable approximation spaces. Since this criterion is not directly applicable to the collocation method, herein it is only possible to report numerical observations.

Throughout this work, the polynomial degrees of an approximation field are chosen to be the same for all parametric directions and the polynomial degrees of the displacement and stress fields are denoted as p_d and p_s, respectively. Besides the choice for p_d and p_s, the possible combinations differ in having the same Bézier mesh or an equal number of control points. Among the combinations

1. $p_d = p_s$, same Bézier mesh / same number of control points $(*)$
2. $p_d = p_s + 1$, same Bézier mesh
3. $p_d = p_s + 1$, same number of control points $(*)$
4. $p_s = p_d + 1$, same Bézier mesh $(*)$
5. $p_s = p_d + 1$, same number of control points

the best results were obtained for the options marked with an asterisk. Therefore, these three options are investigated in this section. For the other two options the errors were several orders of magnitude higher for most of the refinement steps. Therefore we excluded these options. The Bézier meshes and control nets of an example geometry for the combinations marked with an asterisk are shown in figures 2 - 4. For all investigated discretizations the knot vectors are uniform.

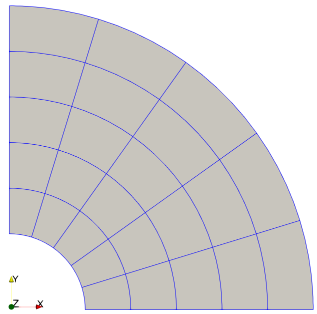

(a) Displacements: Bézier mesh

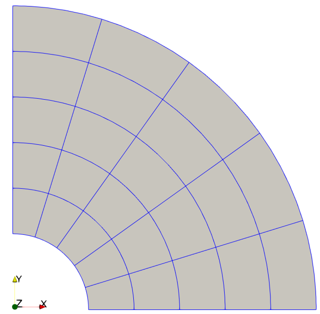

(b) Stresses: Bézier mesh

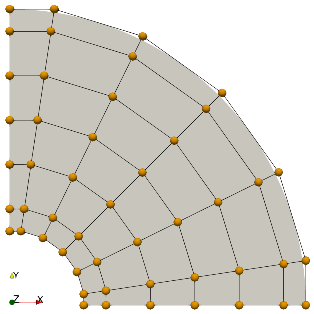

(c) Displacements: Control net

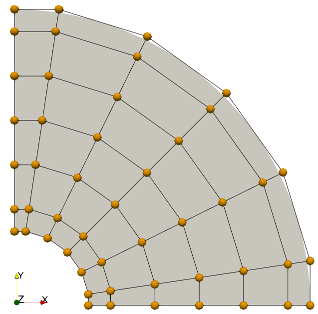

(d) Stresses: Control net

Figure 2: Quarter of annulus: Example for discretization with equal degrees ($p_d = p_s = 2$) and same number of control points ($n_d = n_s = 7$).

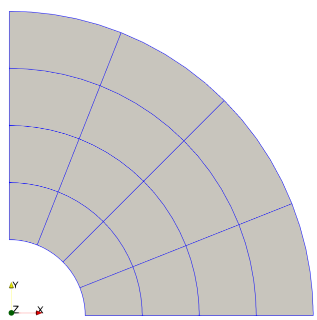

(a) Displacements: Bézier mesh

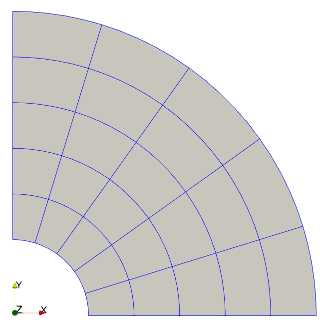

(b) Stresses: Bézier mesh

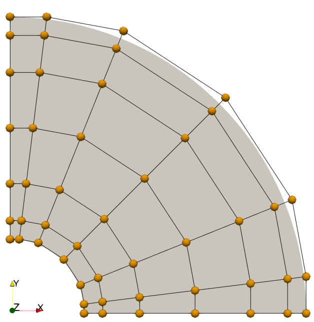

(c) Displacements: Control net

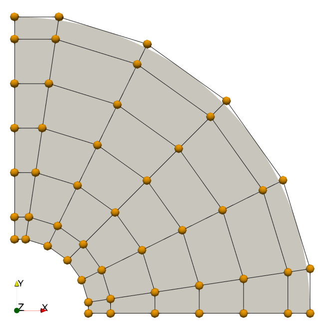

(d) Stresses: Control net

Figure 3: Quarter of annulus: Example for discretization with enriched displacement field ($p_d = p_s + 1 = 3$) and same number of control points ($n_d = n_s = 7$).

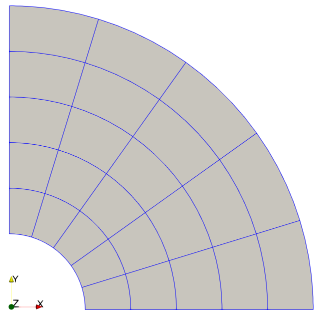

(a) Displacements: Bézier mesh

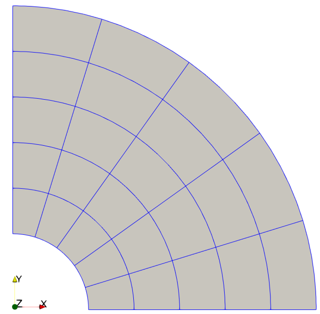

(b) Stresses: Bézier mesh

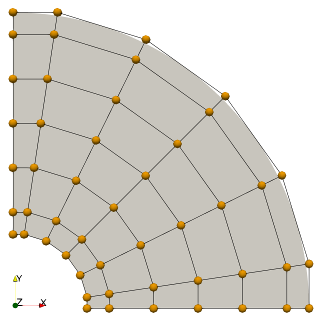

(c) Displacements: Control net

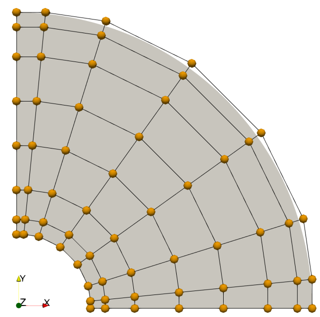

(d) Stresses: Control net

Figure 4: Quarter of annulus: Example for discretization with enriched stress field ($p_s = p_d + 1 = 3$) and same Bézier mesh (number of control points $n_s = n_d + 1 = 8$).

For reasons of comparability, the number of control points in the convergence plots always refers to the displacement approximation space. The relative errors $E_{\boldsymbol{u}}$ and $E_{\boldsymbol{\sigma}}$ of the displacements and stresses, respectively, are reported in terms of the L^2-norm, whenever an analytical solution is available. Due to symmetry of the stress tensor, the shear stress component σ_{yx} is not taken into account for the calculation of the error $E_{\boldsymbol{\sigma}}$.

As described in section 3.5, a hybrid collocation-Galerkin approach is applied to incorporate Neumann boundary conditions. The results from the collocation approach without hybrid treatment of the boundaries are given in the appendix for comparison purposes. For the last example surface plots are shown to visualize field outputs. To capture the general distribution patterns, the colour bar limits are set manually for these plots and thus do not necessarily coincide with the actual data ranges.

4.1. Quarter of annulus with body load

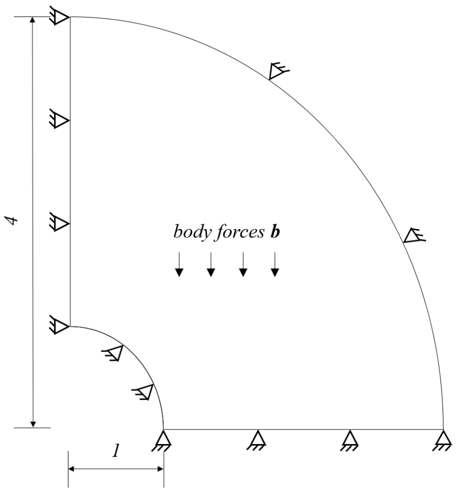

(a) Geometry and boundary conditions

Simulation setup

Number of control points:
$n_d = 10 \times 10 - 160 \times 160$
Polynomial degree:
$p_d/p_s = 2 - 7$
Lamé's first parameter:
$\lambda = 1$ or 10^4
Lamé's second parameter:
$\mu = 1$

(b) Simulation parameters

Figure 5: Quarter of annulus with body load: Geometry, boundary conditions and simulation setup.

For the volumetric locking investigations, a quarter of annulus as illustrated in figure 5 is considered as first benchmark test. The domain is represented by a single patch parameterization and homogeneous Dirichlet boundary conditions are assumed on the whole boundary. Following [18], the pre-defined divergence-free manufactured solution

$$\begin{aligned} u_{1,ref}(x,y) =& 10^{-6}x^2y^4(x^2+y^2-16)(x^2+y^2-1) \\ & (5x^4+18x^2y^2-85x^2+13y^4+80-153y^2), \\ u_{2,ref}(x,y) =& -2\cdot 10^{-6}xy^5(x^2+y^2-16)(x^2+y^2-1) \\ & (5x^4-51x^2+6x^2y^2-17y^2+16+y^4). \end{aligned} \tag{52}$$

is assigned via the corresponding body forces.

As a motivation for the mixed approach and for comparison purposes, the results obtained with a primal collocation approach are reported first. A description of the primal isogeometric collocation method for linear elasticity can, e.g., be found in [18]. Figures 6 and 7 show the relative errors $E_{\boldsymbol{u}}$ and $E_{\boldsymbol{\sigma}}$ of the displacements and stresses. The behaviour for the compressible case is shown on the left-hand side and on the right-hand side the nearly incompressible counterpart is given. There is hardly any convergence detectable for the polynomial degrees $p = 2$ and $p = 3$ and nearly incompressible material behaviour, which indicates volumetric locking issues. Higher polynomial degrees lead to a recovery of the expected convergence rates, however, with errors of two to three orders of magnitude higher for the nearly incompressible case than for the compressible case.

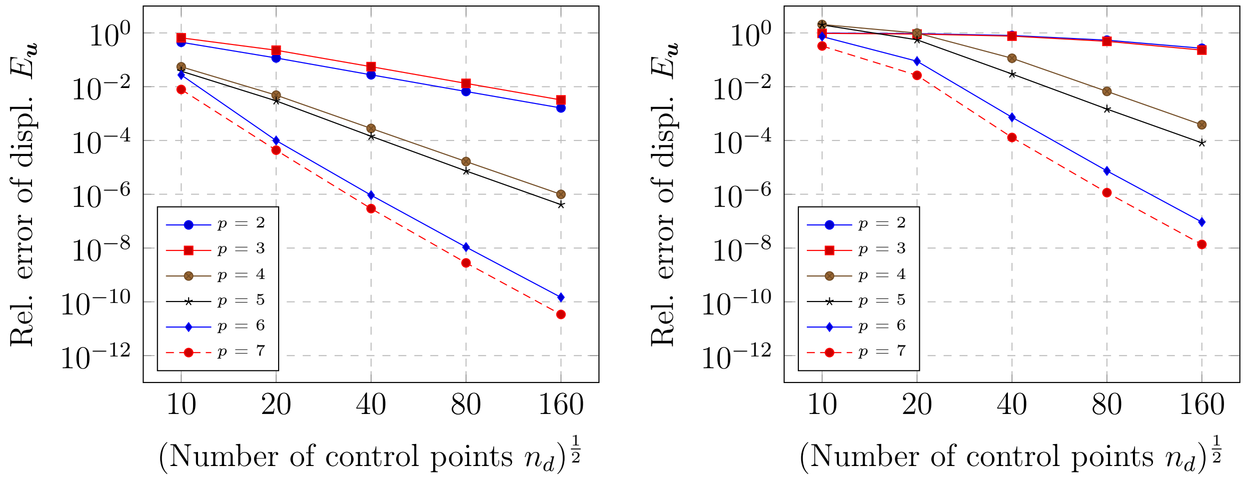

(a) Compressible ($\lambda = 1$)

(b) Nearly incompressible ($\lambda = 10^4$)

Figure 6: Quarter of annulus with body load: Relative error of displacements $E_{\boldsymbol{u}}$, primal collocation method.

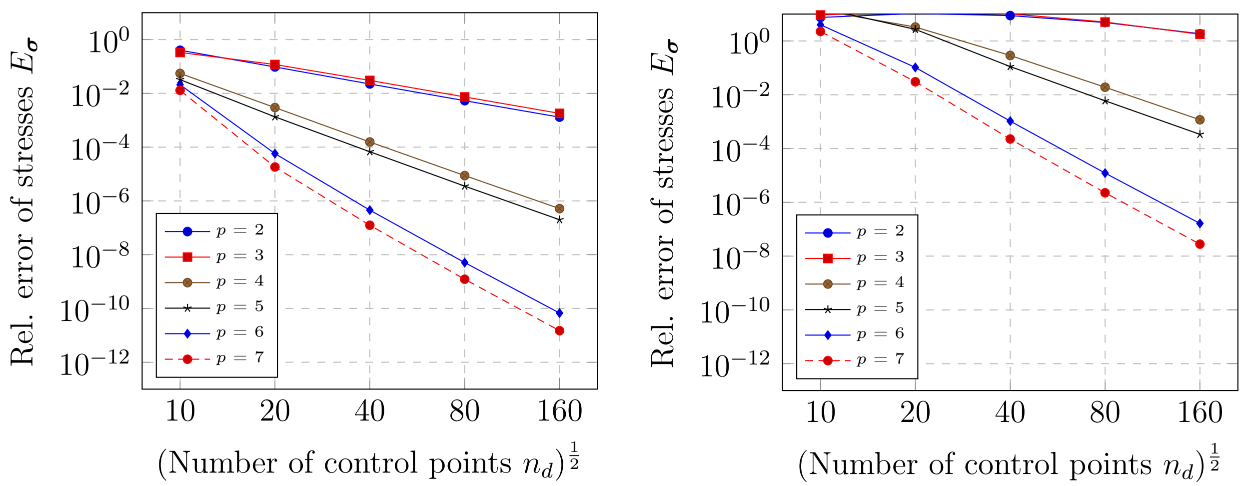

(a) Compressible ($\lambda = 1$)

(b) Nearly incompressible ($\lambda = 10^4$)

Figure 7: Quarter of annulus with body load: Relative error of stresses $E_{\boldsymbol{\sigma}}$, primal collocation method.

In the following, the results for the mixed isogeometric collocation approach are reported. Figures 8 and 9 show the relative errors $E_{\boldsymbol{u}}$ and $E_{\boldsymbol{\sigma}}$ of the displacements and stresses, respectively, for an equal degree approximation ($p_s = p_d$). Regarding the relative error of the displacements, one can observe that the convergence behaviour for the different polynomial degrees is nearly identical for the compressible and the nearly incompressible cases. The relative error of the stresses is slightly larger in the nearly incompressible regime in comparison to the compressible case, but the convergence rates are almost identical. For the highest polynomial degree ($p_d = 7$) and fine discretizations, a slight decrease of the convergence rate is observed in the nearly incompressible case, which might be induced by a higher condition number.

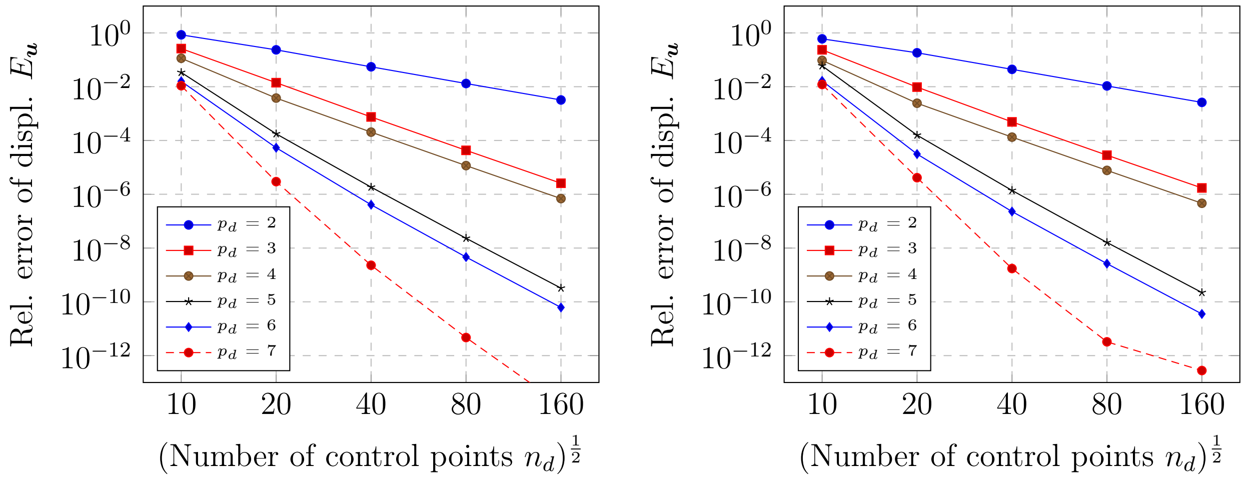

(a) Compressible ($\lambda = 1$)

(b) Nearly incompressible ($\lambda = 10^4$)

Figure 8: Quarter of annulus with body load: Relative error of displacements $E_{\boldsymbol{u}}$, equal degree approximation ($p_s = p_d$).

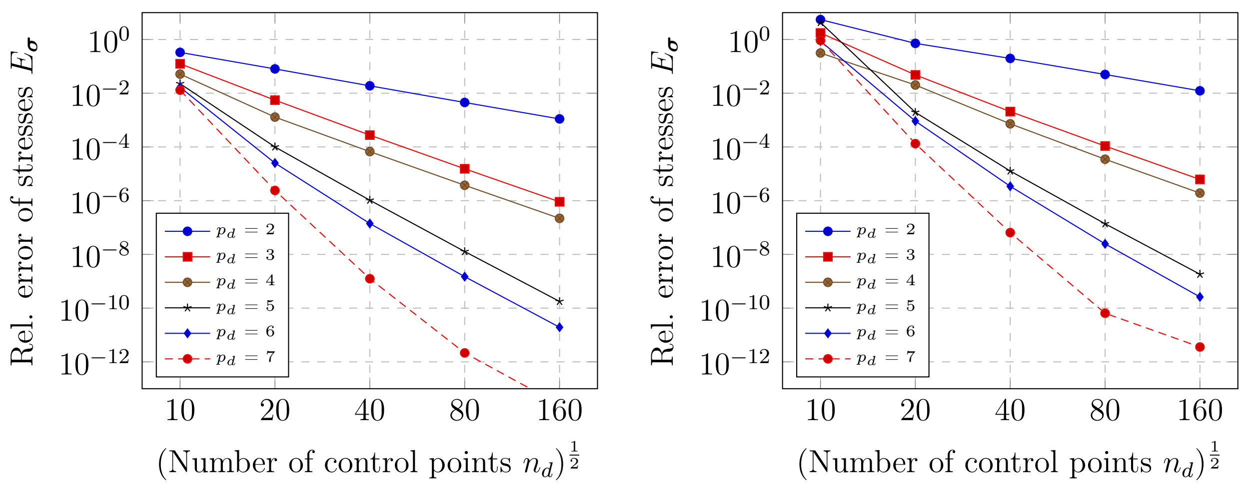

(a) Compressible ($\lambda = 1$)

(b) Nearly incompressible ($\lambda = 10^4$)

Figure 9: Quarter of annulus with body load: Relative error of stresses $E_{\boldsymbol{\sigma}}$, equal degree approximation ($p_s = p_d$).

The corresponding plots for the enriched stress field case ($p_s = p_d + 1$, same Bézier mesh) can be found in figures 10 and 11. Regarding the relative error $E_{\boldsymbol{u}}$, a difference can be observed between even and odd polynomial degrees. The results obtained with even polynomial degrees (of the displacement field) for the compressible case are almost identical to those of the nearly incompressible case. For the odd polynomial degree approximations of the displacement field, the errors are slightly larger in the nearly incompressible regime. The relative errors of the stresses $E_{\boldsymbol{\sigma}}$ are larger in the nearly incompressible case than for compressible material behaviour as it can be observed in figure 11. Despite the larger absolute values, the convergence rates are comparable.

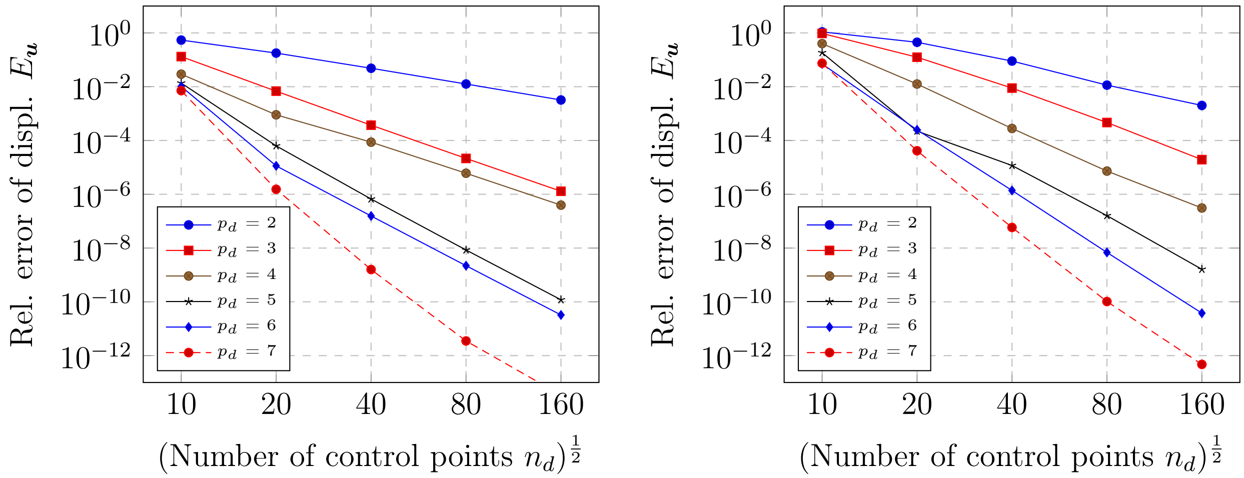

(a) Compressible ($\lambda = 1$)

(b) Nearly incompressible ($\lambda = 10^4$)

Figure 10: Quarter of annulus with body load: Relative error of displacements $E_{\boldsymbol{u}}$, enriched stress field ($p_s = p_d + 1$, same Bézier mesh).

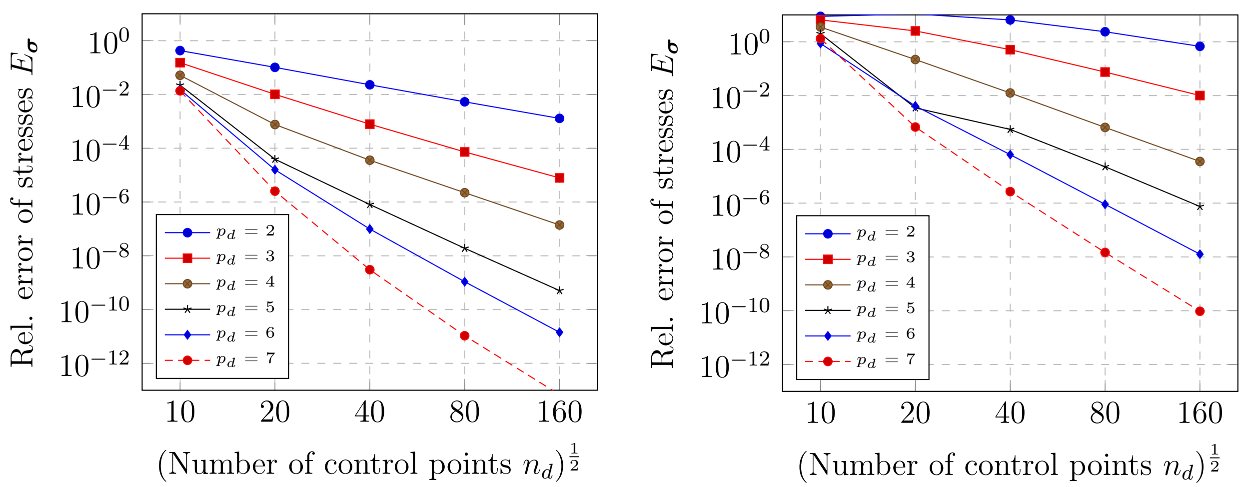

(a) Compressible ($\lambda = 1$)

(b) Nearly incompressible ($\lambda = 10^4$)

Figure 11: Quarter of annulus with body load: Relative error of stresses $E_{\boldsymbol{\sigma}}$, enriched stress field ($p_s = p_d + 1$, same Bézier mesh).

The convergence plots for the combination with the enriched displacement field ($p_d = p_s + 1$) and same number of control points are given in figures 12 and 13. This choice of approximation spaces seems to be the most effective one regarding the treatment of volumetric locking effects for this example. For both evaluated errors there are hardly any differences between the compressible and nearly incompressible regime. Only for the highest polynomial degree ($p_d = 7$) one can note a decrease in the convergence rates in the nearly incompressible regime for fine discretizations as also observed for the equal degree discretizations.

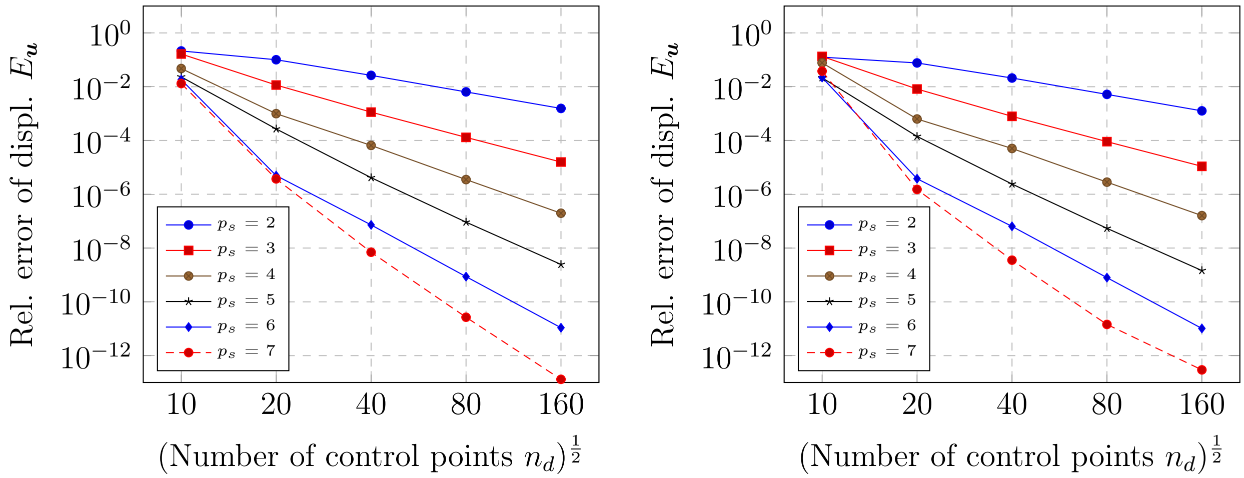

(a) Compressible ($\lambda = 1$)

(b) Nearly incompressible ($\lambda = 10^4$)

Figure 12: Quarter of annulus with body load: Relative error of displacements $E_{\boldsymbol{u}}$, enriched displacement field ($p_d = p_s + 1$, same number of control points).

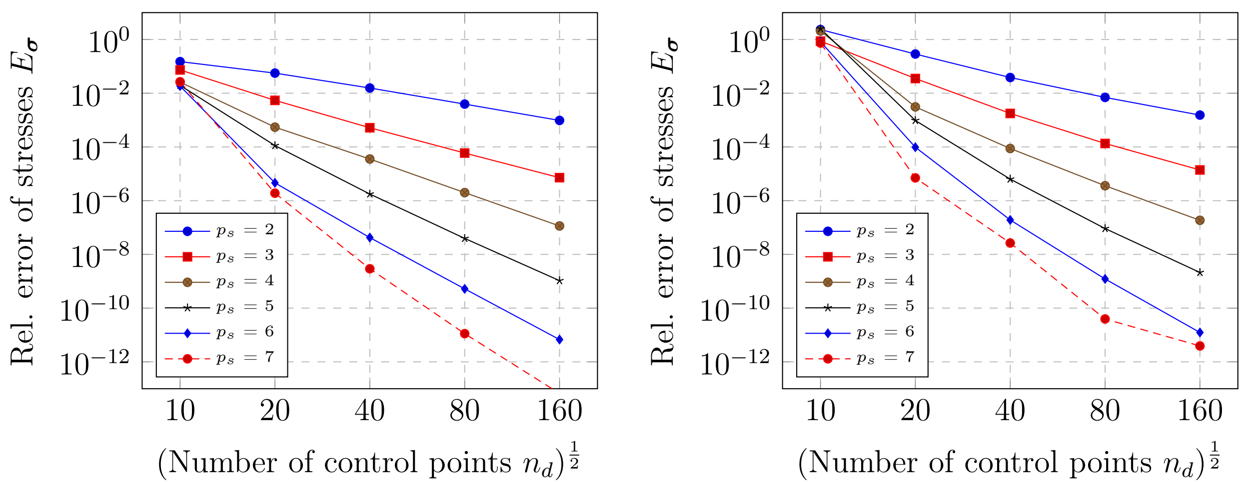

(a) Compressible ($\lambda = 1$)

(b) Nearly incompressible ($\lambda = 10^4$)

Figure 13: Quarter of annulus with body load: Relative error of stresses $E_{\boldsymbol{\sigma}}$, enriched displacement field ($p_d = p_s + 1$, same number of control points).

4.2. Pressurized thick-walled cylinder

The second numerical example consists of a pressurized thick-walled cylinder. The geometry, boundary conditions and simulation parameters can be found in figure 14. Due to symmetry it is sufficient to model only one quarter of the cylinder. A constant pressure $p = 15/8$ is applied to the inner wall. The material parameters and investigated discretizations are identical to those of the previous example.

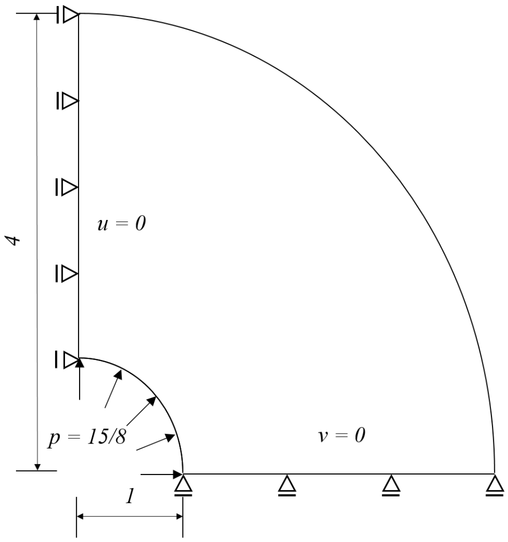

(a) Geometry and boundary conditions

Simulation setup

Number of control points:
$n_d = 10 \times 10 - 160 \times 160$
Polynomial degree:
$p_d / p_s = 2 - 7$
Lamé's first parameter:
$\lambda = 1$ or 10^4
Lamé's second parameter:
$\mu = 1$

(b) Simulation parameters

Figure 14: Pressurized thick-walled cylinder: Geometry, boundary conditions and simulation setup.

The convergence plots for the equal degree discretizations can be found in figures 15 and 16. Compared to the results of the equal degree case in the first example, the difference between the compressible and nearly incompressible regime is more pronounced in this example, but the general trend is the same. This also applies to the results obtained without the hybrid treatment of the boundaries as shown in figures A.1 and A.2 in the appendix.

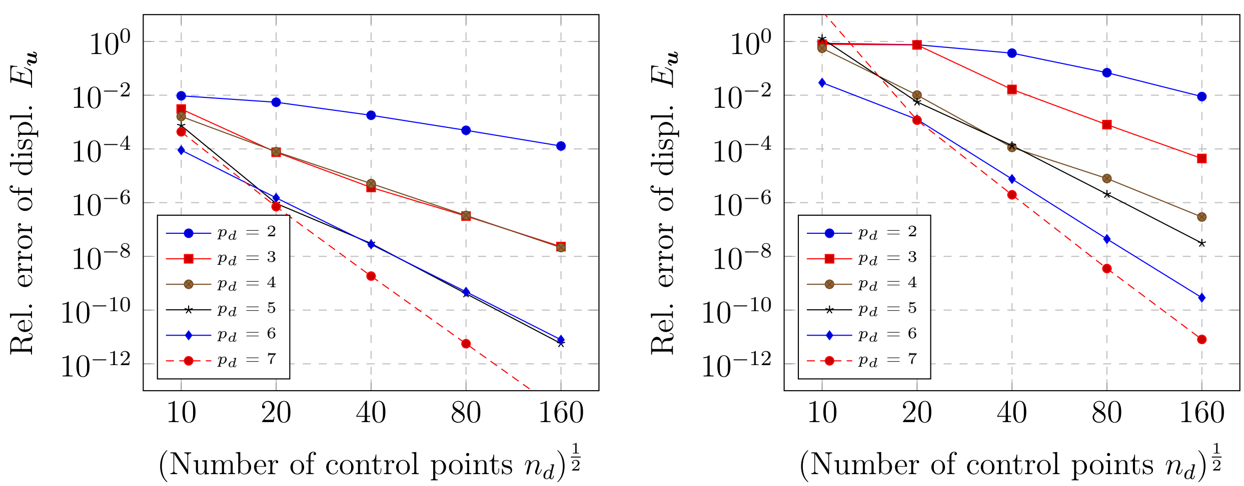

(a) Compressible ($\lambda = 1$)

(b) Nearly incompressible ($\lambda = 10^4$)

Figure 15: Pressurized thick-walled cylinder: Relative error of displacements $E_{\boldsymbol{u}}$, equal degree approximation ($p_s = p_d$), hybrid approach.

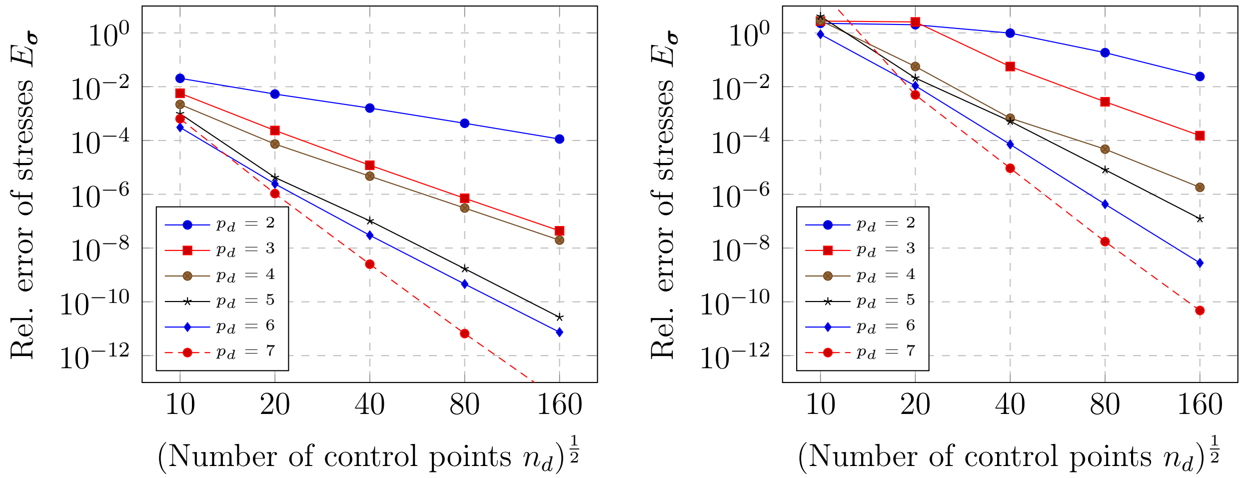

(a) Compressible ($\lambda = 1$)

(b) Nearly incompressible ($\lambda = 10^4$)

Figure 16: Pressurized thick-walled cylinder: Relative error of stresses $E_{\boldsymbol{\sigma}}$, equal degree approximation ($p_s = p_d$), hybrid approach.

Also for the discretization approach with an enriched stress field ($p_s = p_d+1$, same Bézier mesh), the results differ significantly between the compressible and nearly incompressible regime as it can be seen in figures 17 and 18. In the nearly incompressible regime the errors are about three orders of magnitude higher than in the compressible regime for nearly all tested discretizations with the enriched stress field approach. The hybrid approach seems to have a mild positive effect on the solution. This can be seen by looking at the results without hybrid approach, which are shown in the appendix in figures A.3 and A.4.

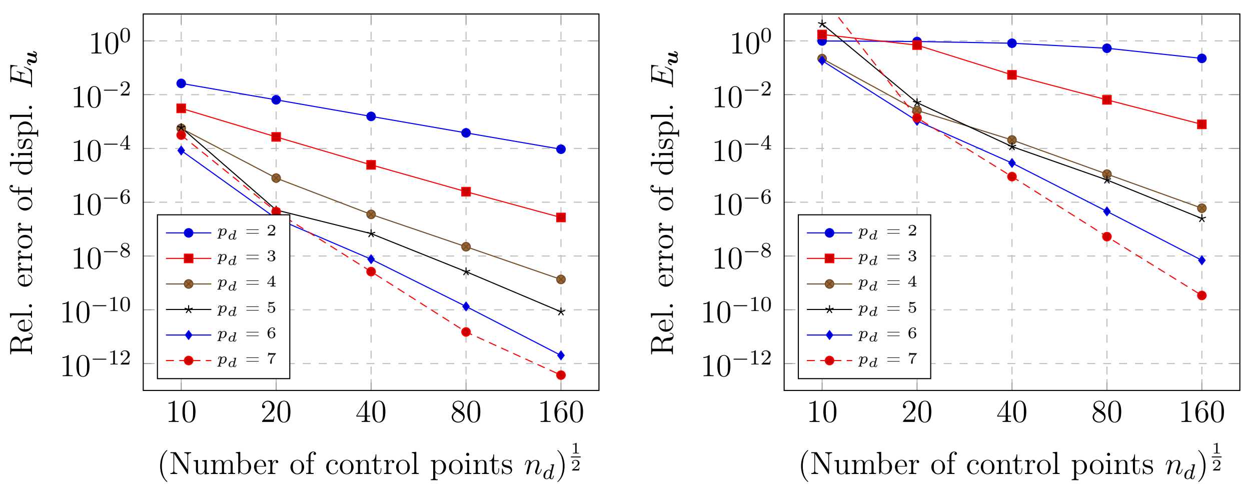

(a) Compressible ($\lambda = 1$)

(b) Nearly incompressible ($\lambda = 10^4$)

Figure 17: Pressurized thick-walled cylinder: Relative error of displacements $E_{\boldsymbol{u}}$, enriched stress field ($p_s = p_d + 1$, same Bézier mesh), hybrid approach.

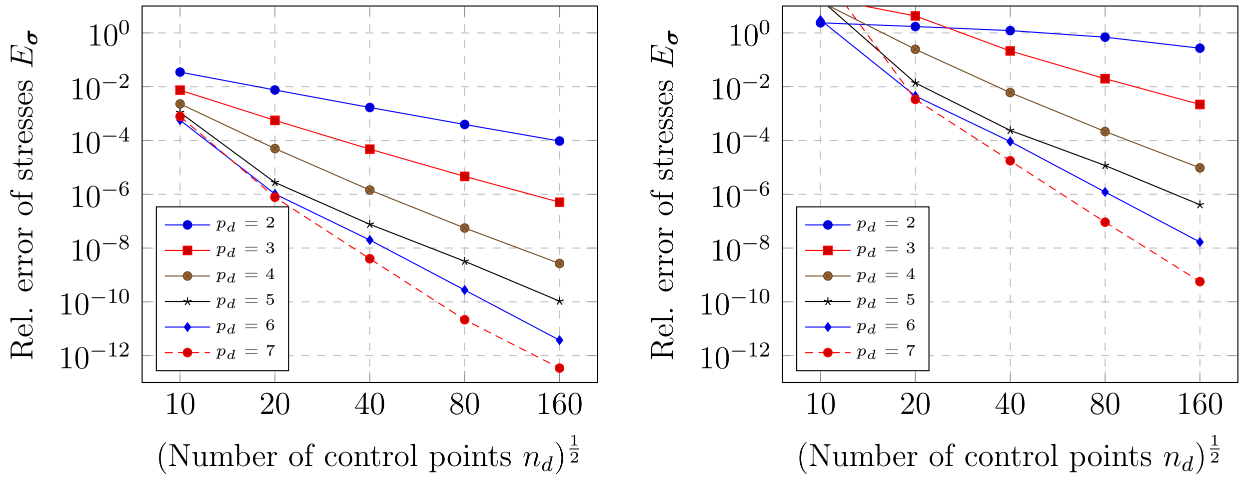

(a) Compressible ($\lambda = 1$)

(b) Nearly incompressible ($\lambda = 10^4$)

Figure 18: Pressurized thick-walled cylinder: Relative error of stresses $E_{\boldsymbol{\sigma}}$, enriched stress field ($p_s = p_d + 1$, same Bézier mesh), hybrid approach.

In figures 19 and 20 the convergence plots for the combination with an enriched displacement field ($p_d = p_s + 1$, same number of control points) are given. The results of the compressible and nearly incompressible cases are nearly identical, except for discretizations with coarse Bézier meshes. A similar behaviour can be observed for this choice of discretization in the first benchmark test as well. Only for the highest polynomial degree tested ($p_s = 7$) and a fine Beziér mesh, the error rises in the nearly incompressible regime, once again possibly due to high condition numbers. The results are comparable if no hybrid approach is used as shown in figures A.5 and A.6 in the appendix.

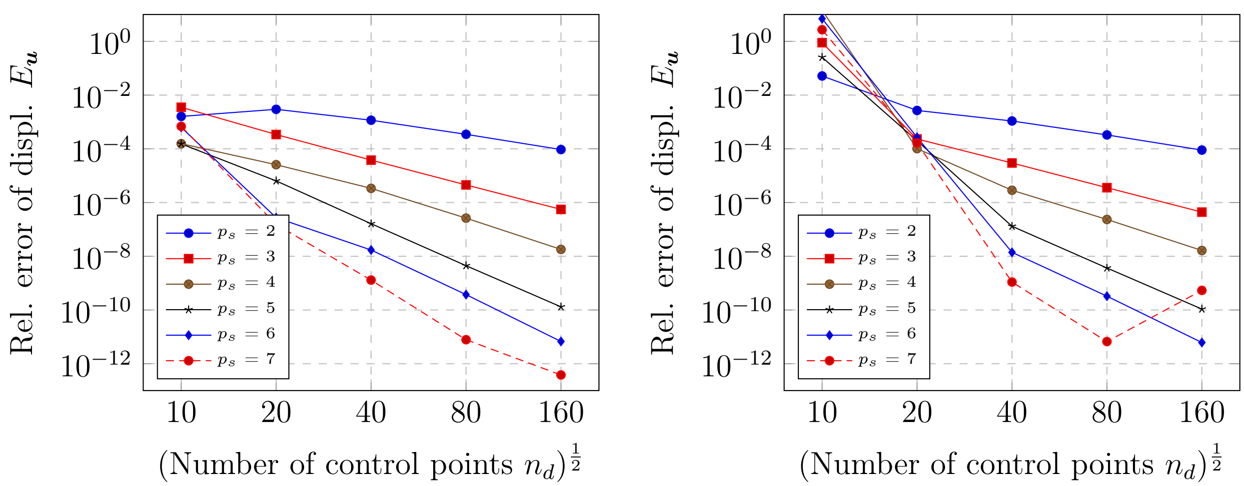

(a) Compressible ($\lambda = 1$)

(b) Nearly incompressible ($\lambda = 10^4$)

Figure 19: Pressurized thick-walled cylinder: Relative error of displacements $E_{\boldsymbol{u}}$, enriched displacement field ($p_d = p_s + 1$, same number of control points), hybrid approach.

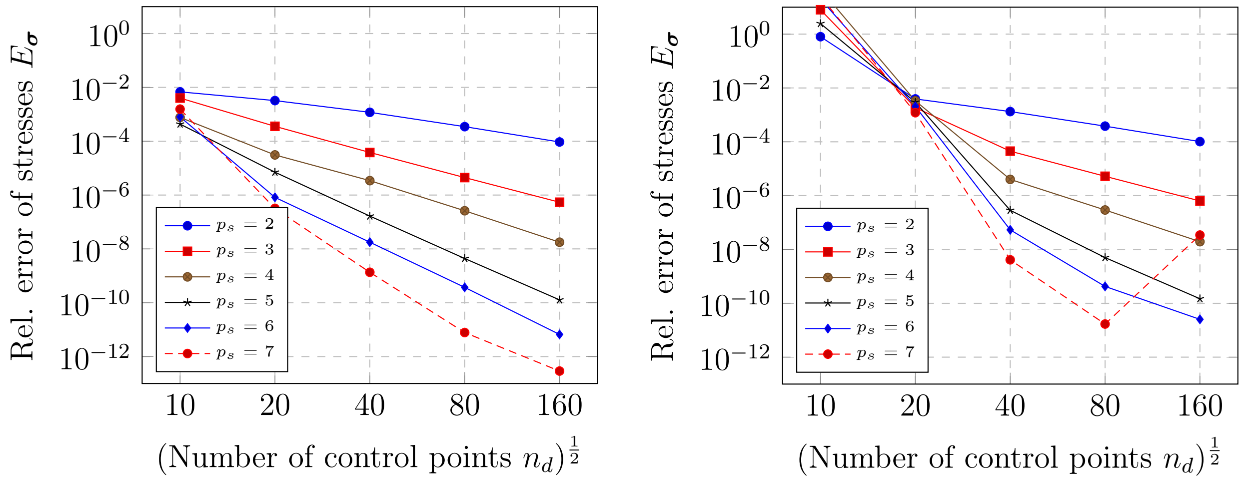

(a) Compressible ($\lambda = 1$)

(b) Nearly incompressible ($\lambda = 10^4$)

Figure 20: Pressurized thick-walled cylinder: Relative error of stresses $E_{\boldsymbol{\sigma}}$, enriched displacement field ($p_d = p_s + 1$, same number of control points), hybrid approach.

4.3. Cook's membrane

The third numerical example in this section is the well-known Cook's membrane. The material parameters are chosen as described in [43] and given in figure 21 along with the geometry, boundary conditions and further simulation parameters. The left-hand side of the geometry is fully clamped and a tangential traction $q = 6.25$ is enforced on the right-hand side. The vertical displacement of point A is studied in the following. The results are compared to those of a displacement-based Galerkin method, since no analytical solution exists.

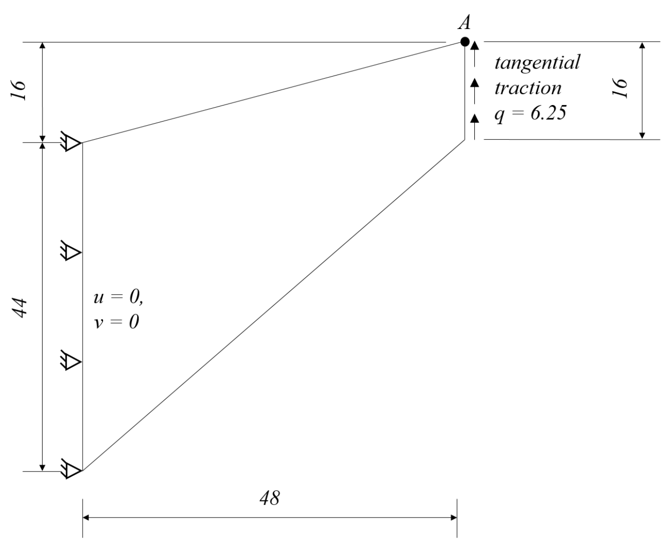

Simulation setup

Number of control points:
$n_d = 10 \times 10 - 150 \times 150$
Polynomial degree:
$p_d/p_s/p = 2 - 7$
Young's modulus:
$E = 240.565$
Poisson's ratio:
$\nu = 0.3$ or 0.4999

(a) Geometry and boundary conditions

(b) Simulation parameters

Figure 21: Cook's membrane: Geometry, boundary conditions and simulation setup.

The convergence plots for the equal degree discretizations can be found in figure 22. For the compressible case, both Galerkin and the collocation method converge quickly to a constant value as expected. Only the collocation method with the lowest polynomial degree ($p_d = 2, p_s = 2$) seems to converge slower. In case of nearly incompressible material behaviour, the results for the tested discretizations show larger discrepancies. For the lowest polynomial degree, both Galerkin and collocation converge slowly. For the other degrees, collocation converges faster than Galerkin in most cases. The corresponding plots for the collocation approach without hybrid treatment of the boundaries can be found in figure A.7 of the appendix. In the compressible regime, the convergence behaviour of the collocation method is slower in almost all cases if no hybrid treatment of the boundaries is performed. For the nearly incompressible case, reasonably accurate results can only be obtained for the lowest polynomial degree ($p_d = 2, p_s = 2$), thus the hybrid approach seems to have a stabilizing effect. For all other tested discretizations, the results obtained without hybrid approach are out of the data range of the plot.

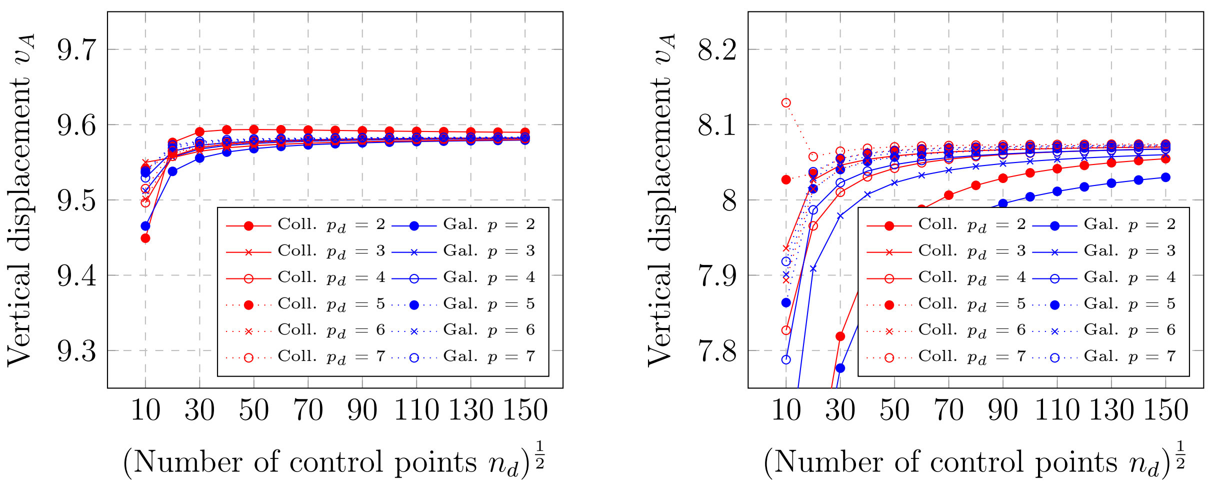

(a) Compressible ($\nu = 0.3$)

(b) Nearly incompressible ($\nu = 0.4999$)

Figure 22: Cook's membrane: Vertical displacement of top right corner (point A), equal degree approximation ($p_s = p_d$), hybrid approach.

For the discretization approach with an enriched stress field ($p_s = p_d + 1$, same Bézier mesh), the results differ clearly between the compressible and nearly incompressible cases as one can see in figure 23. For the compressible case, the proposed approach converges quickly except for the lowest polynomial degree ($p_d = 2, p_s = 3$). Only a few discretizations converge in the nearly incompressible case. Without hybrid treatment of the Neumann boundaries (see figure A.8 in the appendix), none of the tested discretizations converges in the nearly incompressible regime and the results for the compressible case are also significantly worse in comparison to those obtained with the hybrid approach.

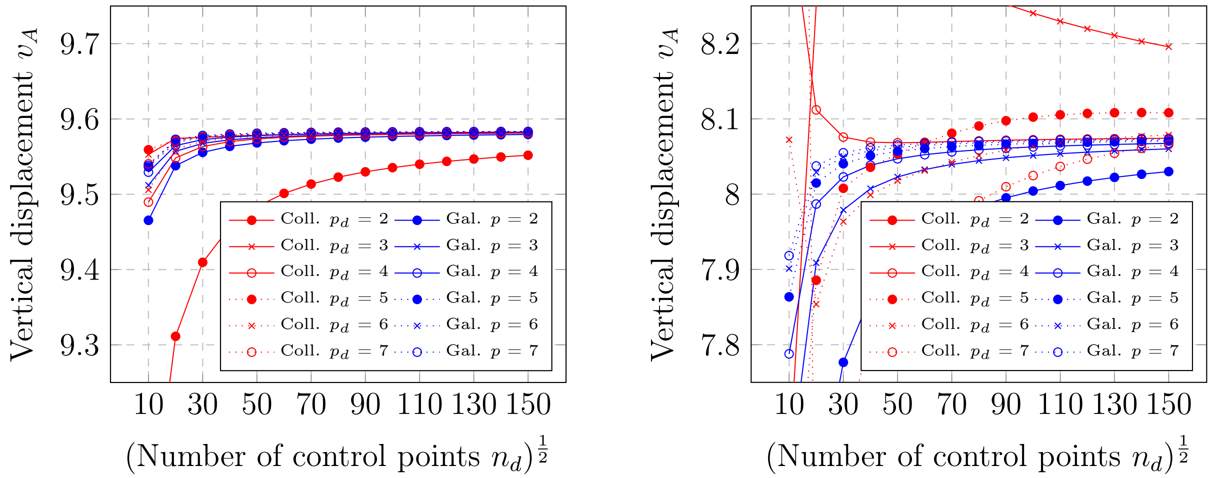

(a) Compressible ($\nu = 0.3$) (b) Nearly incompressible ($\nu = 0.4999$)

Figure 23: Cook's membrane: Vertical displacement of top right corner (point A), enriched stress field ($p_s = p_d + 1$, same Bézier mesh), hybrid approach.

Again the approach with an enriched displacement field ($p_d = p_s + 1$, same number of control points) delivers the most accurate results as shown in figure 24. Both for compressible and nearly incompressible material behaviour, the solutions converge fast to a constant value. This holds also true for the same approach without hybrid treatment, but a spurious jump occurs for a discretization of $n_d = 70$ and $p_s = 4$ and the errors for coarse Bézier meshes are comparatively large. The corresponding results obtained without hybrid treatment of the boundaries are reported in figure A.9.

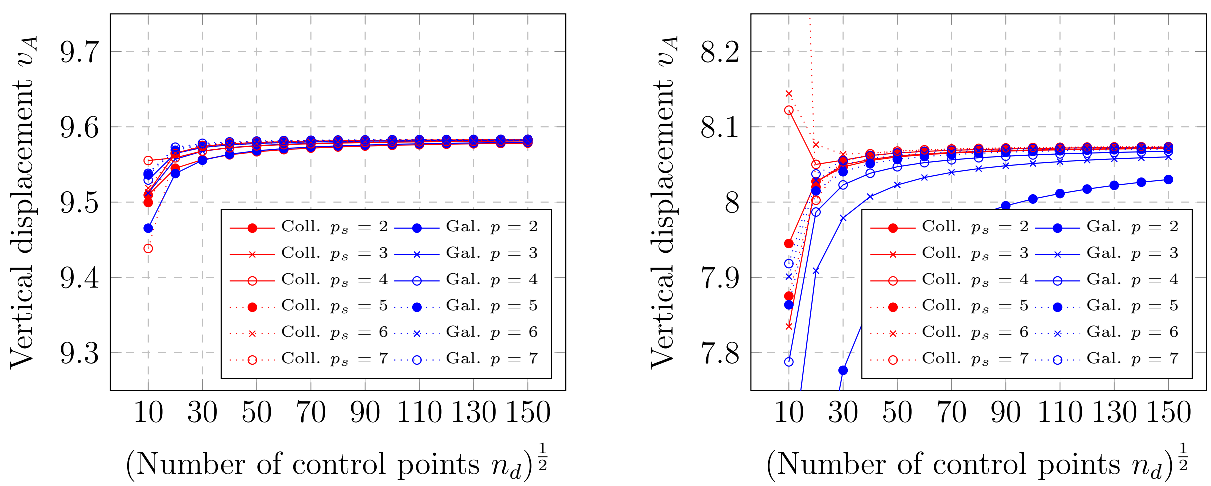

(a) Compressible ($\nu = 0.3$) (b) Nearly incompressible ($\nu = 0.4999$)

Figure 24: Cook's membrane: Vertical displacement of top right corner (point A), enriched displacement field ($p_d = p_s + 1$, same number of control points), hybrid approach.

In addition, plots of the stresses for Galerkin and mixed collocation ($p_d = p_s + 1$, same number of control points) discretizations with $n_d = 100$ and different polynomial degrees can be found in figures A.10 - A.15 in the appendix. For the mixed collocation approach, minor oscillations are noticeable both in the compressible and nearly incompressible regime. With the Galerkin approach, oscillations are not visible for compressible materials, but significantly large oscillations occur in the nearly incompressible regime, especially for $p = 2$.

5. Numerical examples on elastoplasticity

In this section the application of the mixed isogeometric collocation formulation to three problems of elastoplasticity is shown. For each example the results of the proposed mixed isogeometric collocation method are compared to displacement-based Galerkin results, which are treated as reference solutions. For all numerical examples plane strain conditions and von Mises plasticity with isotropic hardening are assumed. The elastoplastic constitutive equations are integrated in time via a classical return-mapping algorithm as described in section 2.3.

For the mixed isogeometric collocation method, solely the approximation spaces with enriched displacement field ($p_d = p_s + 1$, same number of control points) are used, since they show the best performance in the numerical examples of the previous section 4. As mentioned in the previous section, the polynomial degrees p_d and p_s of the displacement and stress fields, respectively, are chosen to be the same for all parametric directions. The initial guess of the Newton-Raphson method at each load step is linearly extrapolated from the previous load step. For all examples the equivalent plastic strain distributions are reported. Since these values are only available at the collocation / quadrature points, a projection to the corresponding space is carried out to visualise the results. In addition the stresses are plotted for the last examples. As in the previous section, the colour bar limits are set manually to capture the general distribution patterns and thus do not necessarily coincide with the actual data ranges.

5.1. Quarter of annulus

As first example a quarter of annulus as depicted in figure 25 is simulated. A total horizontal displacement $u = 0.05$ at the bottom edge is applied incrementally within 20 load steps, afterwards the specimen is unloaded in the same manner. The additional boundary conditions and further simulation parameters are reported in figure 25.

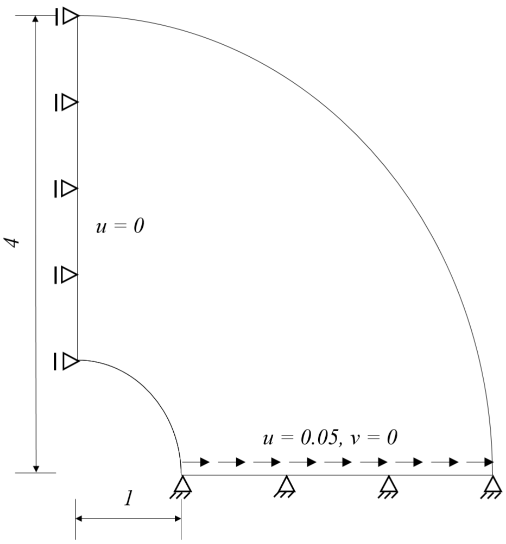

(a) Geometry and boundary conditions

Simulation setup

Number of control points $n_d = 50 \times 50$
Polynomial degree $p_s/p = 2 - 7$
Load increments $= 20$
Total displacement $u = 0.05$
Young's modulus $E = 200$
Poisson's ratio $\nu = 0.3$
Yield stress $\sigma_y = 1$
Hardening modulus $K = 20$

(b) Simulation parameters

Figure 25: Quarter of annulus: Geometry, boundary conditions and simulation setup.

From the results of the load-displacement curves in figure 26, where the load is computed from the reaction forces at the lower edge, one can deduce that there is a perfect agreement between the proposed mixed collocation approach and the Galerkin reference solutions, both in the loading and unloading phases.

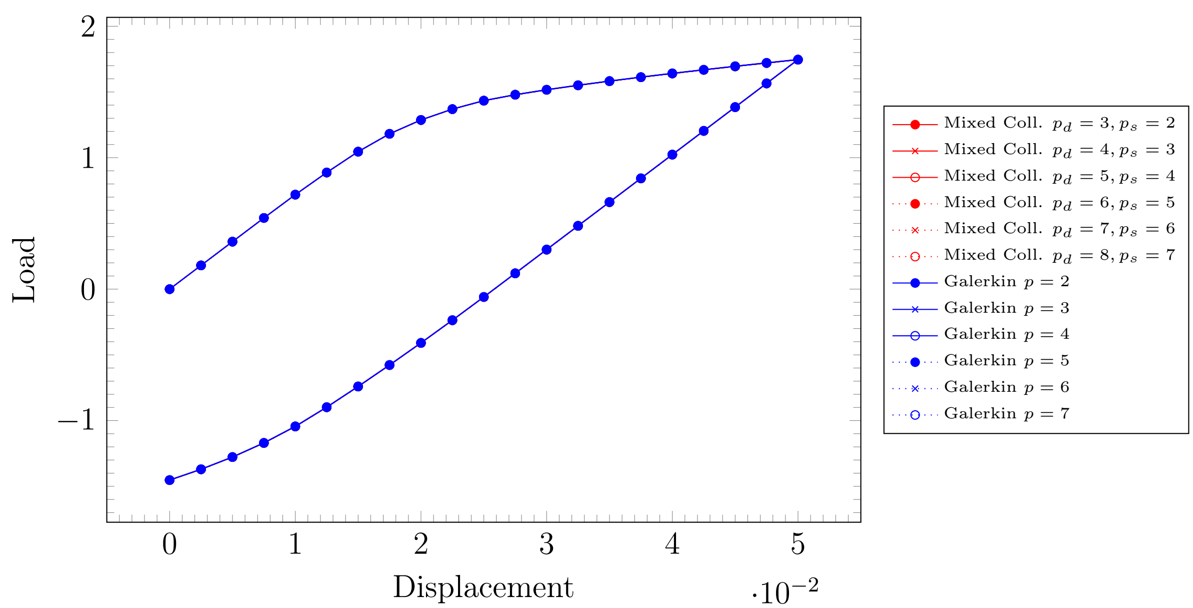

Figure 26: Quarter of annulus: Load-displacement curves.

Figure 27, which illustrates the equivalent plastic strains at the last load step (end of the unloading phase) calculated via both the mixed collocation and the Galerkin approaches, confirms the positive conclusions drawn from the load-displacements curves. Except for mild oscillations observed for the mixed collocation approach in case of the discretization with low polynomial degree ($p_d = 3, p_s = 2$), there is an excellent agreement between the results of the proposed collocation approach and the reference solution in the equivalent plastic strain distributions. The maximum equivalent plastic strains are concentrated at the bottom corner points. Another plastic front evolves from the top part of the circular hole. The corresponding plots for the end of the loading phase can be found in figure A.16 in the appendix.

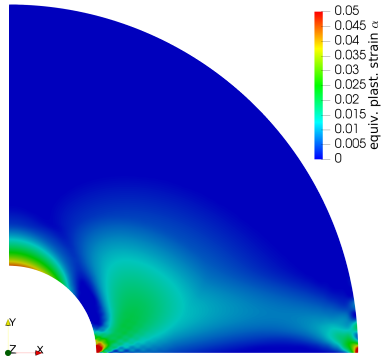

(a) Mixed Collocation ($p_d = 3, p_s = 2$)

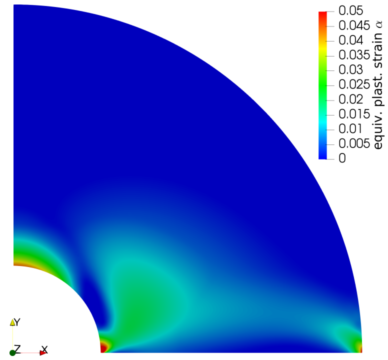

(b) Galerkin ($p = 2$)

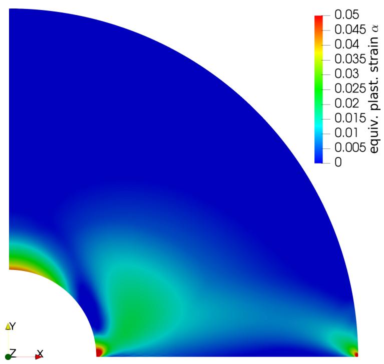

(c) Mixed Collocation ($p_d = 8, p_s = 7$)

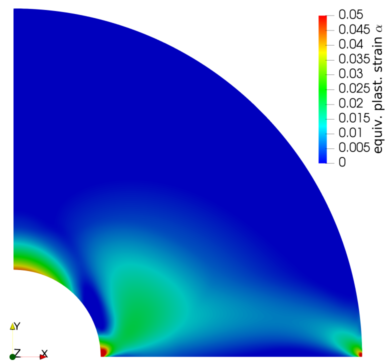

(d) Galerkin ($p = 7$)

Figure 27: Quarter of annulus: Equivalent plastic strain α, load step 40.

5.2. Clamped tensile test

As second example a square plate is analysed, with boundary conditions and simulation parameters given in figure 28. The lower and upper edges are fully clamped and a total displacement $v = 0.03$ in the vertical direction is imposed on the upper edge. The displacement is applied incrementally within 40 load steps in total for the loading and unloading phase.

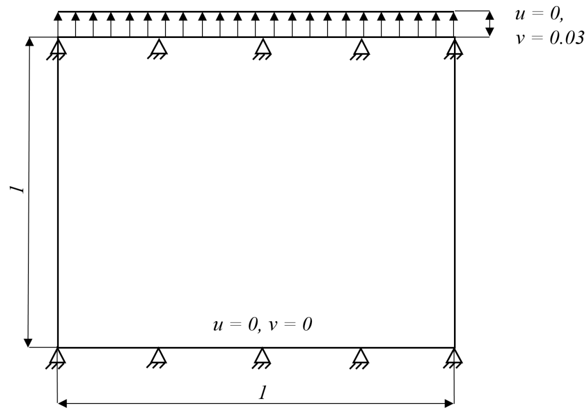

(a) Geometry and boundary conditions

Simulation setup

Number of control points $n_d = 50 \times 50$
Polynomial degree $p_s/p = 2 - 7$
Load increments $= 20$
Total displacement $v = 0.03$
Young's modulus $E = 200$
Poisson's ratio $\nu = 0.3$
Yield stress $\sigma_y = 1$
Hardening modulus $K = 20$

(b) Simulation parameters

Figure 28: Clamped tensile test: Geometry, boundary conditions and simulation setup.

The load-displacement curves, where the load is calculated from the reaction forces at the upper edge, are shown in figure 29. The plots exhibit in general a good agreement between the mixed collocation approach and the Galerkin reference solutions. In the elastic regime hardly any difference is visible and only slight deviations can be detected when plasticity occurs. Only for the discretization with $p_d = 6, p_s = 5$ convergence issues in the unloading phase at a load step with a displacement of $v = 0.012$ occurred. The Newton-Raphson method was stagnating in this load step and also a finer load step increment could not improve the convergence behaviour. Therefore the solution for this specific discretization is only reported up to the point where the non-convergence issues are observed.

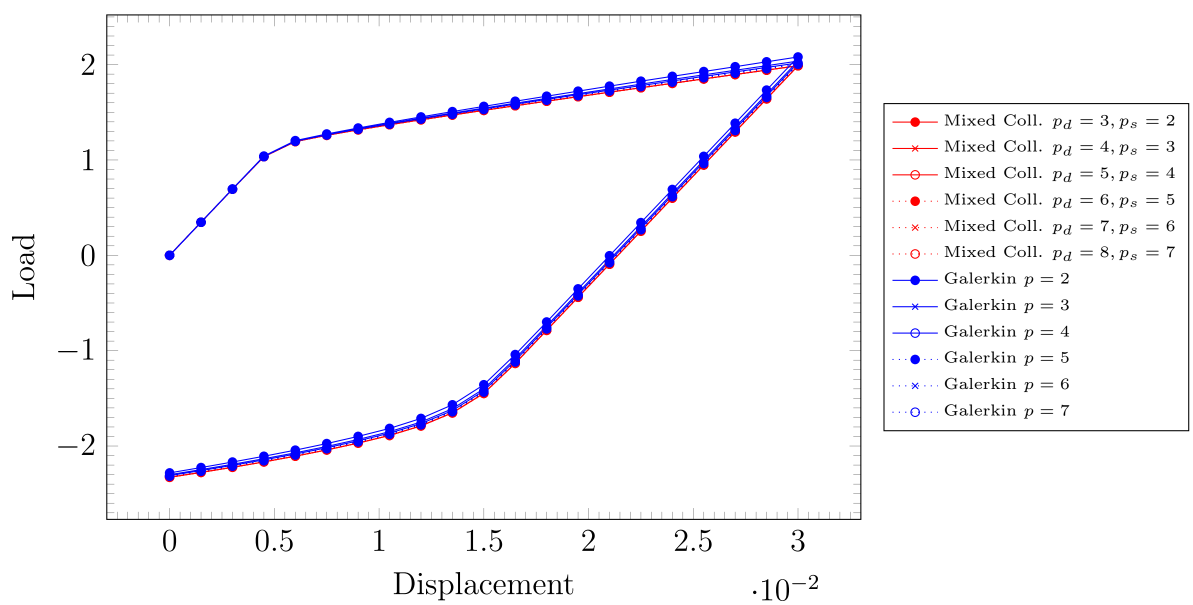

Figure 29: Clamped tensile test: Load-displacement curves.

Figure 30 shows the equivalent plastic strain distributions after complete unloading, whereas the same plot at full loading (after 20 load steps) can be found in figure A.17 in the appendix. Similar equivalent plastic strain patterns can be observed for the collocation and the Galerkin methods, but mild oscillations occur in the mixed collocation solution for the discretization with the lowest polynomial degree ($p_d = 3, p_s = 2$). The oscillations are more pronounced in the corner regions, where the highest stresses arise. For discretizations with a high polynomial degree (e.g. $p_d = 8, p_s = 7$ in figure 30), these oscillations are not visible anymore. This effect is similar to that observed in the previous example.

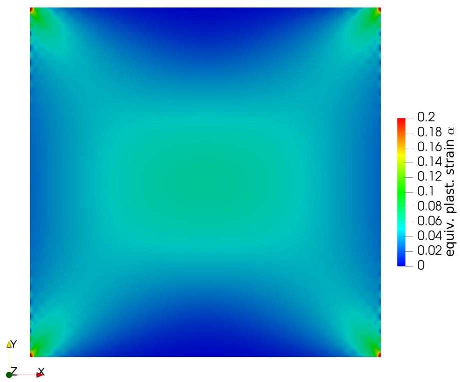

(a) Mixed Collocation ($p_d = 3, p_s = 2$)

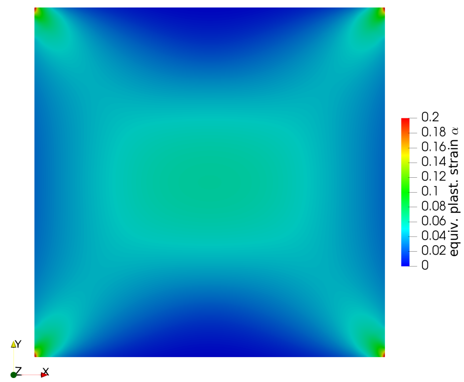

(b) Galerkin ($p = 2$)

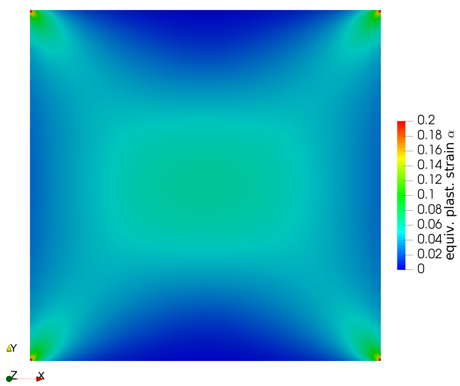

(c) Mixed Collocation ($p_d = 8, p_s = 7$)

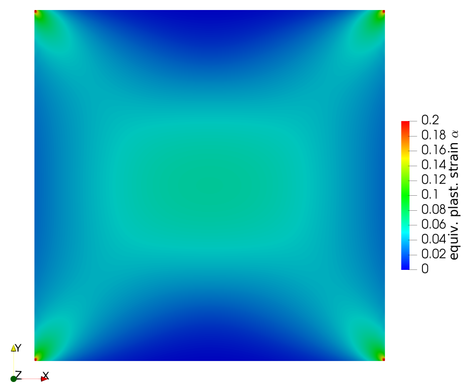

(d) Galerkin ($p = 7$)

Figure 30: Clamped tensile test: Equivalent plastic strain α, load step 40.

5.3. Plate with circular hole

The last example consists of a plate with circular hole. Due to symmetry, only one quarter of the plate is modelled. The geometry definition, boundary conditions and further simulation parameters are depicted in figure 31.

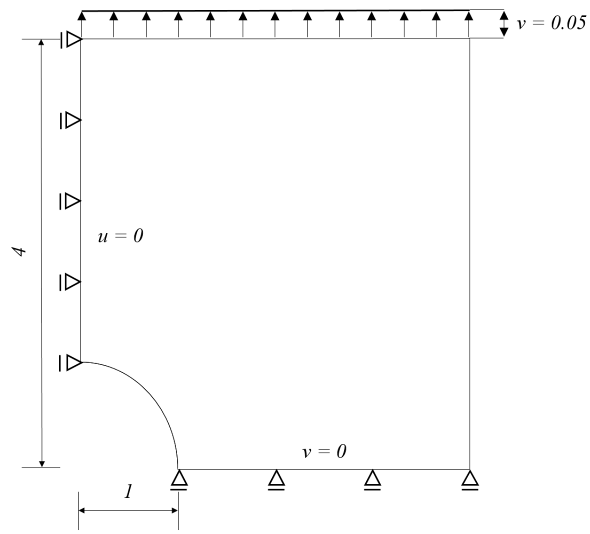

(a) Geometry and boundary conditions

Simulation setup

Number of control points $n_d = 50 \times 50$
Polynomial degree $p_s/p = 2 - 7$
Load increments $= 20$
Total displacement $v = 0.05$
Young's modulus $E = 200$
Poisson's ratio $\nu = 0.3$
Yield stress $\sigma_y = 1$
Hardening modulus $K = 20$

(b) Simulation parameters

Figure 31: Plate with circular hole: Geometry, boundary conditions and simulation setup.

In the isogeometric literature there exist different strategies to model the sharp, upper right corner of this geometry. In this work a multi-patch approach is used to maintain a regular Bézier mesh and to test the applicability of the approach for multi-patch parameterizations. The geometry consists of two patches, as depicted in figure 32, with 50 control points in each parametric direction per patch.

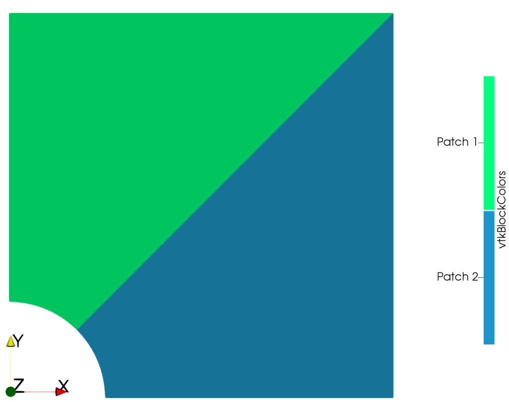

Figure 32: Plate with circular hole: Conforming multi-patch parameterization.

The load-displacement curves obtained with the mixed collocation method are plotted in figure 33 and exactly match the corresponding results of the Galerkin reference solution for all discretizations. This indicates that also multi-patch parameterizations and thus more complex structures can be simulated by the proposed approach.

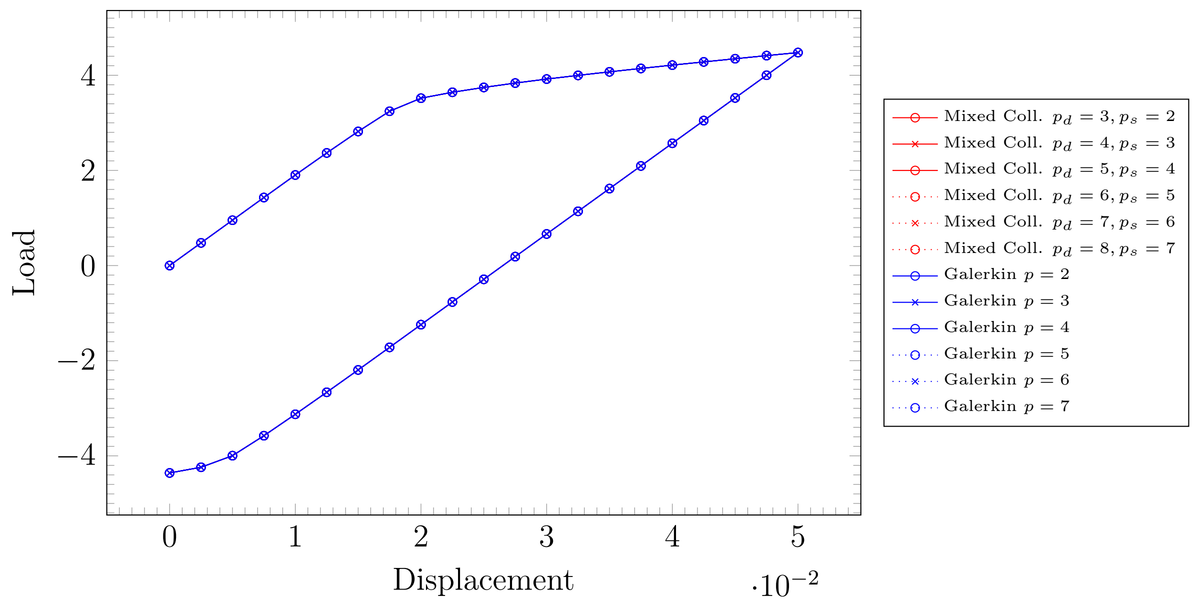

Figure 33: Plate with circular hole: Load-displacement curves.

An equally good agreement is indicated by the plots of the equivalent plastic strains in figure 34, where there are hardly any deviations between the results of the proposed isogeometric collocation approach and the Galerkin reference solutions. The equivalent plastic strain distribution between the two patches is smooth and no influence of the coupling can be observed. The same holds for the distribution at the state of maximum loading (after 20 load steps), which can be found in figure A.18 in the appendix.

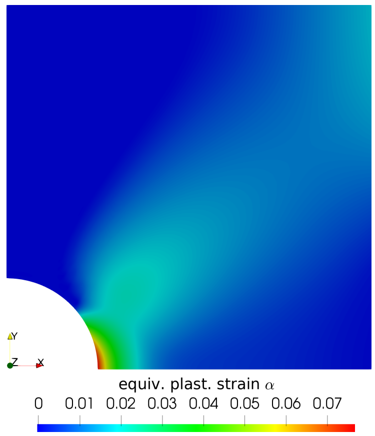

(a) Mixed Collocation ($p_d = 3, p_s = 2$)

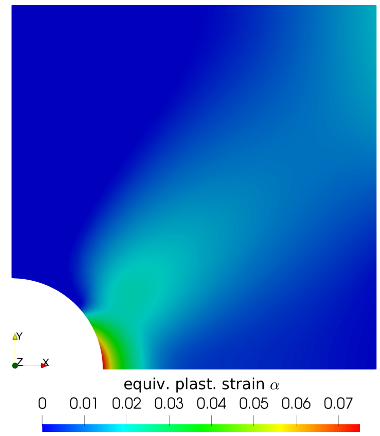

(b) Galerkin ($p = 2$)

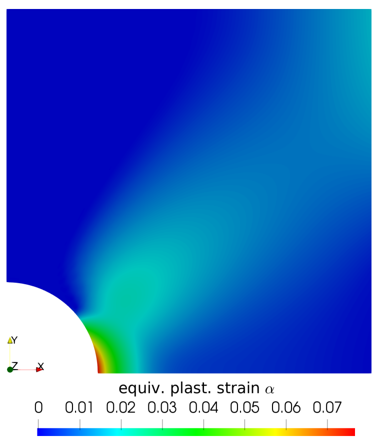

(c) Mixed Collocation ($p_d = 8, p_s = 7$)

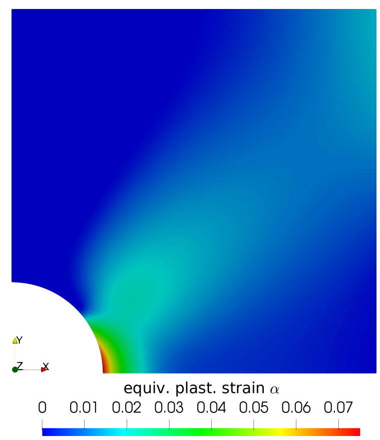

(d) Galerkin ($p = 7$)

Figure 34: Plate with circular hole: Equivalent plastic strain α, load step 40.

Additionally, the stress distribution at the final state can be seen in figures A.19-A.21 in the appendix. As outlined in section 3.6, the patch coupling is performed via the displacement DOFs, which may raise the question of the smoothness of the obtained stress fields at the patch boundaries. In figures A.19-A.21, which can be found in the appendix, the stress distribution patterns are smooth, including the common edge of the two patches. This holds true for all the components of the stress tensor.

6. Summary and conclusions

A mixed stress-displacement isogeometric collocation method for nearly incompressible elastic and elastoplastic materials was proposed in this work. Various numerical examples were investigated, in which results of the proposed approach were compared with analytical or displacement-based Galerkin reference solutions.

In the first part of the paper volumetric locking effects in nearly incompressible elasticity were investigated. The proposed mixed isogeometric collocation formulation was tested with three different choices of approximation spaces. Based on the obtained results, the best choice seems to be a discretization of the displacement field with one degree higher than that of the stress field, but with the same number of control points. Additionally, a hybrid collocation-Galerkin treatment of the Neumann boundaries had a positive effect on the stability and accuracy. With this discretization setup, results were hardly affected by the degree of compressibility of the material.

In the second part of this work von Mises elastoplasticity was addressed. There the discretization with an enriched displacement field was used a priori. The proposed mixed method circumvents the stability issues of the primal collocation formulation for plasticity. It led to load-displacement curves and equivalent plastic strain fields which were in excellent agreement with the reference results from a classical Galerkin scheme. Also in this case, a hybrid collocation-Galerkin approach (Galerkin for the momentum balance equation and collocation for the stress coupling equation) was applied to improve the accuracy of the results. In addition the extension of the approach to conforming multi-patch parameterizations, based on a coupling of the displacement DOFs at the common boundaries, was investigated. The obtained displacement and stress fields showed a smooth transition between adjacent boundaries.

7. Acknowledgement

FF and LDL gratefully acknowledge the financial support of the German Research Foundation (DFG) within the DFG Priority Program SPP 1748 “Reliable Simulation Techniques in Solid Mechanics”. SM gratefully acknowledges the GNCS - INdAM 2018 project “Model reduction in medical applications”. AR gratefully acknowledges the financial support of the Italian Ministry for Education, University and Research (MIUR) through the PRIN project XFAST-SIMS (no. 20173C478N).

8. Bibliography

[1] T. J. Hughes, J. A. Cottrell, Y. Bazilevs, Isogeometric analysis: CAD, finite elements, NURBS, exact geometry and mesh refinement, Computer Methods in Applied Mechanics and Engineering 194 (39-41) (2005) 4135–4195.

[2] J. A. Cottrell, T. J. Hughes, Y. Bazilevs, Isogeometric Analysis: Toward Integration of CAD and FEA, John Wiley & Sons, 2009.

[3] T. J. Hughes, A. Reali, G. Sangalli, Efficient quadrature for NURBS-based isogeometric analysis, Computer Methods in Applied Mechanics and Engineering 199 (5-8) (2010) 301–313.

[4] F. Auricchio, F. Calabro, T. J. Hughes, A. Reali, G. Sangalli, A simple algorithm for obtaining nearly optimal quadrature rules for NURBS-based isogeometric analysis, Computer Methods in Applied Mechanics and Engineering 249 (2012) 15–27.

[5] D. Schillinger, S. J. Hossain, T. J. Hughes, Reduced Bézier element quadrature rules for quadratic and cubic splines in isogeometric analysis, Computer Methods in Applied Mechanics and Engineering 277 (2014) 1–45.

[6] C. Adam, T. J. Hughes, S. Bouabdallah, M. Zarroug, H. Maitournam, Selective and reduced numerical integrations for NURBS-based isogeometric analysis, Computer Methods in Applied Mechanics and Engineering 284 (2015) 732–761.

[7] M. Bartoň, V. M. Calo, Optimal quadrature rules for odd-degree spline spaces and their application to tensor-product-based isogeometric analysis, Computer Methods in Applied Mechanics and Engineering 305 (2016) 217–240.

[8] R. R. Hiemstra, F. Calabro, D. Schillinger, T. J. Hughes, Optimal and reduced quadrature rules for tensor product and hierarchically refined splines in isogeometric analysis, Computer Methods in Applied Mechanics and Engineering 316 (2017) 966–1004.

[9] K. A. Johannessen, Optimal quadrature for univariate and tensor product splines, Computer Methods in Applied Mechanics and Engineering 316 (2017) 84–99.

[10] V. Puzyrev, Q. Deng, V. Calo, Dispersion-optimized quadrature rules for isogeometric analysis: Modified inner products, their dispersion properties, and optimally blended schemes, Computer Methods in Applied Mechanics and Engineering 320 (2017) 421–443.

[11] Q. Deng, M. Bartoň, V. Puzyrev, V. Calo, Dispersion-minimizing quadrature rules for C1 quadratic isogeometric analysis, Computer Methods in Applied Mechanics and Engineering 328 (2018) 554–564.

[12] A. Karatarakis, P. Karakitsios, M. Papadrakakis, GPU accelerated computation of the isogeometric analysis stiffness matrix, Computer Methods in Applied Mechanics and Engineering 269 (2014) 334–355.

[13] P. Antolin, A. Buffa, F. Calabro, M. Martinelli, G. Sangalli, Efficient matrix computation for tensor-product isogeometric analysis: The use of sum factorization, Computer Methods in Applied Mechanics and Engineering 285 (2015) 817–828.

[14] F. Calabro, G. Sangalli, M. Tani, Fast formation of isogeometric Galerkin matrices by weighted quadrature, Computer Methods in Applied Mechanics and Engineering 316 (2017) 606–622.

[15] A. Mantzaflaris, B. Jüttler, B. N. Khoromskij, U. Langer, Low rank tensor methods in Galerkin-based isogeometric analysis, Computer Methods in Applied Mechanics and Engineering 316 (2017) 1062–1085.

[16] G. Sangalli, M. Tani, Matrix-free weighted quadrature for a computationally efficient isogeometric k-method, Computer Methods in Applied Mechanics and Engineering 338 (2018) 117–133.

[17] F. Auricchio, L. B. Da Veiga, T. J. Hughes, A. Reali, G. Sangalli, Isogeometric collocation methods, Mathematical Models and Methods in Applied Sciences 20 (11) (2010) 2075–2107.

[18] F. Auricchio, L. B. Da Veiga, T. J. Hughes, A. Reali, G. Sangalli, Isogeometric collocation for elastostatics and explicit dynamics, Computer Methods in Applied Mechanics and Engineering 249 (2012) 2–14.

[19] D. Schillinger, J. A. Evans, A. Reali, M. A. Scott, T. J. Hughes, Isogeometric collocation: Cost comparison with Galerkin methods and extension to adaptive hierarchical NURBS discretizations, Computer Methods in Applied Mechanics and Engineering 267 (2013) 170–232.

[20] R. Kruse, N. Nguyen-Thanh, L. De Lorenzis, T. J. Hughes, Isogeometric collocation for large deformation elasticity and frictional contact problems, Computer Methods in Applied Mechanics and Engineering 296 (2015) 73–112.

[21] A. Reali, T. J. Hughes, An introduction to isogeometric collocation methods, in: Isogeometric Methods for Numerical Simulation, Springer, 2015, pp. 173–204.

[22] L. De Lorenzis, J. Evans, T. J. Hughes, A. Reali, Isogeometric collocation: Neumann boundary conditions and contact, Computer Methods in Applied Mechanics and Engineering 284 (2015) 21–54.

[23] J. Kiendl, E. Marino, L. De Lorenzis, Isogeometric collocation for the Reissner–Mindlin shell problem, Computer Methods in Applied Mechanics and Engineering 325 (2017) 645–665.

[24] J. A. Evans, R. R. Hiemstra, T. J. Hughes, A. Reali, Explicit higher-order accurate isogeometric collocation methods for structural dynamics, Computer Methods in Applied Mechanics and Engineering 338 (2018) 208–240.

[25] J. Kiendl, F. Auricchio, A. Reali, A displacement-free formulation for the Timoshenko beam problem and a corresponding isogeometric collocation approach, Meccanica 53 (6) (2018) 1403–1413.

[26] E. Marino, J. Kiendl, L. De Lorenzis, Explicit isogeometric collocation for the dynamics of three-dimensional beams undergoing finite motions, Computer Methods in Applied Mechanics and Engineering 343 (2019) 530–549.

[27] E. Marino, J. Kiendl, L. De Lorenzis, Isogeometric collocation for implicit dynamics of three-dimensional beams undergoing finite motions, Computer Methods in Applied Mechanics and Engineering 356 (2019) 548–570.

[28] C. Anitescu, Y. Jia, Y. J. Zhang, T. Rabczuk, An isogeometric collocation method using superconvergent points, Computer Methods in Applied Mechanics and Engineering 284 (2015) 1073–1097.

[29] H. Gomez, L. De Lorenzis, The variational collocation method, Computer Methods in Applied Mechanics and Engineering 309 (2016) 152–181.

[30] M. Montardini, G. Sangalli, L. Tamellini, Optimal-order isogeometric collocation at Galerkin superconvergent points, Computer Methods in Applied Mechanics and Engineering 316 (2017) 741–757.

[31] F. Maurin, F. Greco, S. Dedoncker, W. Desmet, Isogeometric analysis for nonlinear planar Kirchhoff rods: weighted residual formulation and collocation of the strong form, Computer Methods in Applied Mechanics and Engineering.

[32] F. Fahrendorf, L. De Lorenzis, H. Gomez, Reduced integration at superconvergent points in isogeometric analysis, Computer Methods in Applied Mechanics and Engineering 328 (2018) 390–410.

[33] J. C. Simo, T. J. Hughes, Computational Inelasticity, Vol. 7, Springer Science & Business Media, 2006.

[34] E. A. de Souza Neto, D. Peric, D. R. Owen, Computational Methods for Plasticity: Theory and Applications, John Wiley & Sons, 2011.

[35] M. Wilkins, L. L. Laboratory, B. L. R. L. University of California, Calculation of elastic-plastic flow, University of California Lawrence Radiation Laboratory, 1963.

[36] R. D. Krieg, D. Krieg, Accuracies of Numerical Solution Methods for the Elastic-Perfectly Plastic Model, Journal of Pressure Vessel Technology 99 (4) (1977) 510–515.

[37] J. C. Simo, R. L. Taylor, Consistent tangent operators for rate-independent elastoplasticity, Computer Methods in Applied Mechanics and Engineering 48 (1) (1985) 101–118.

[38] R. P. Cardoso, J. Cesar de Sa, The enhanced assumed strain method for the isogeometric analysis of nearly incompressible deformation of solids, International Journal for Numerical Methods in Engineering 92 (1) (2012) 56–78.

[39] T. Elguedj, Y. Bazilevs, V. M. Calo, T. J. Hughes, B-bar an F-bar projection methods for nearly incompressible linear and non-linear elasticity and plasticity using higher-order NURBS elements, Computer Methods in Applied Mechanics and Engineering 197 (33-40) (2008) 2732–2762.

[40] T. Elguedj, T. J. Hughes, Isogeometric analysis of nearly incompressible large strain plasticity, Computer Methods in Applied Mechanics and Engineering 268 (2014) 388–416.

[41] R. Taylor, Isogeometric analysis of nearly incompressible solids, International Journal for Numerical Methods in Engineering 87 (1-5) (2011) 273–288.

[42] K. M. Mathisen, K. M. Okstad, T. Kvamsdal, S. B. Raknes, Isogeometric analysis of finite deformation nearly incompressible solids, Journal of Structural Mechanics 44 (3) (2011) 260–278.

[43] C. Kadapa, W. Dettmer, D. Perić, Subdivision based mixed methods for isogeometric analysis of linear and nonlinear nearly incompressible materials, Computer Methods in Applied Mechanics and Engineering 305 (2016) 241–270.

[44] S. Morganti, F. Fahrendorf, L. De Lorenzis, J. A. Evans, T. J. Hughes, A. Reali, Isogeometric collocation: A mixed u/p method for nearly incompressible elasticity (in preparation).

[45] J. Simo, J. Kennedy, R. Taylor, Complementary mixed finite element formulations for elastoplasticity, Computer Methods in Applied Mechanics and Engineering 74 (2) (1989) 177–206.

[46] J. Schröder, M. Igelbüscher, A. Schwarz, G. Starke, A Prange–Hellinger–Reissner type finite element formulation for small strain elasto-plasticity, Computer Methods in Applied Mechanics and Engineering 317 (2017) 400–418.

[47] R. Bouclier, T. Elguedj, A. Combescure, Development of a mixed displacement-stress formulation for the analysis of elastoplastic structures under small strains: Application to a locking-free, NURBS-based solid-shell element, Computer Methods in Applied Mechanics and Engineering 295 (2015) 543–561.

[48] J. Kiendl, F. Auricchio, L. B. da Veiga, C. Lovadina, A. Reali, Isogeometric collocation methods for the Reissner–Mindlin plate problem, Computer Methods in Applied Mechanics and Engineering 284 (2015) 489–507.

[49] F. Auricchio, L. B. da Veiga, J. Kiendl, C. Lovadina, A. Reali, Isogeometric collocation mixed methods for rods, Discrete and Continuous Dynamical Systems-Series S 9 (1) (2016) 33–42.

[50] O. Weeger, S.-K. Yeung, M. L. Dunn, Isogeometric collocation methods for Cosserat rods and rod structures, Computer Methods in Applied Mechanics and Engineering 316 (2017) 100–122.

[51] G. Balduzzi, S. Morganti, F. Auricchio, A. Reali, Non-prismatic Timoshenko-like beam model: Numerical solution via isogeometric collocation, Computers & Mathematics with Applications 74 (7) (2017) 1531–1541.

[52] S. Morganti, C. Callari, F. Auricchio, A. Reali, Mixed isogeometric collocation methods for the simulation of poromechanics problems in 1D, Meccanica 53 (6) (2018) 1441–1454.

[53] B. Oesterle, S. Bieber, R. Sachse, E. Ramm, M. Bischoff, Intrinsically locking-free formulations for isogeometric beam, plate and shell analysis, PAMM 18 (1) (2018) e201800399.

[54] C. Hesch, P. Betsch, Isogeometric analysis and domain decomposition methods, Computer Methods in Applied Mechanics and Engineering 213 (2012) 104–112.

[55] M. Ruess, D. Schillinger, A. I. Oezcan, E. Rank, Weak coupling for isogeometric analysis of non-matching and trimmed multi-patch geometries, Computer Methods in Applied Mechanics and Engineering 269 (2014) 46–71.

[56] A. Apostolatos, R. Schmidt, R. Wüchner, K.-U. Bletzinger, A Nitsche-type formulation and comparison of the most common domain decomposition methods in isogeometric analysis, International Journal for Numerical Methods in Engineering 97 (7) (2014) 473–504.

[57] E. Brivadis, A. Buffa, B. Wohlmuth, L. Wunderlich, Isogeometric mortar methods, Computer Methods in Applied Mechanics and Engineering 284 (2015) 292–319.

[58] W. Dornisch, J. Stöckler, R. Müller, Dual and approximate dual basis functions for B-splines and NURBS–Comparison and application for an efficient coupling of patches with the isogeometric mortar method, Computer Methods in Applied Mechanics and Engineering 316 (2017) 449–496.

[59] Z. Zou, M. Scott, M. Borden, D. Thomas, W. Dornisch, E. Brivadis, Isogeometric Bézier dual mortaring: Refineable higher-order spline dual bases and weakly continuous geometry, Computer Methods in Applied Mechanics and Engineering 333 (2018) 497–534.

[60] L. Piegl, W. Tiller, The NURBS book, Springer Science & Business Media, 2012.

[61] D. Schillinger, M. J. Borden, H. K. Stolarski, Isogeometric collocation for phase-field fracture models, Computer Methods in Applied Mechanics and Engineering 284 (2015) 583–610.

[62] M. Kapl, V. Vitrih, Isogeometric collocation on planar multi-patch domains, Computer methods in applied mechanics and engineering 360 (2020) 112684.

Appendix A. Additional ressources

Appendix A.1. Additional error plots for the pressurized cylinder (without hybrid approach)

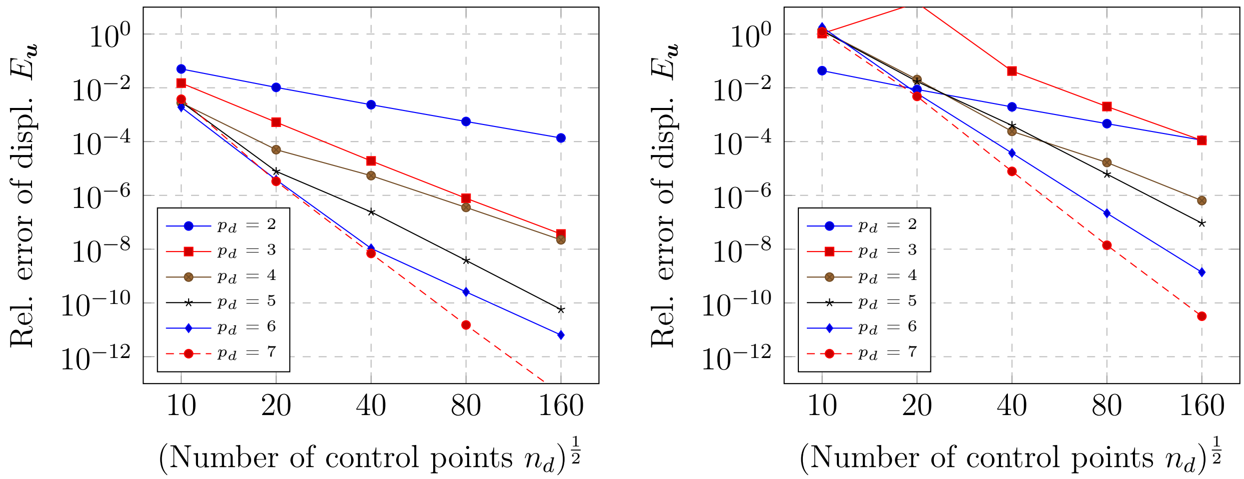

(a) Compressible ($\lambda = 1$)

(b) Nearly incompressible ($\lambda = 10^4$)

Figure A.1: Pressurized thick-walled cylinder: Relative error of displacements $E_{\boldsymbol{u}}$, equal degree approximation ($p_s = p_d$), without hybrid approach.

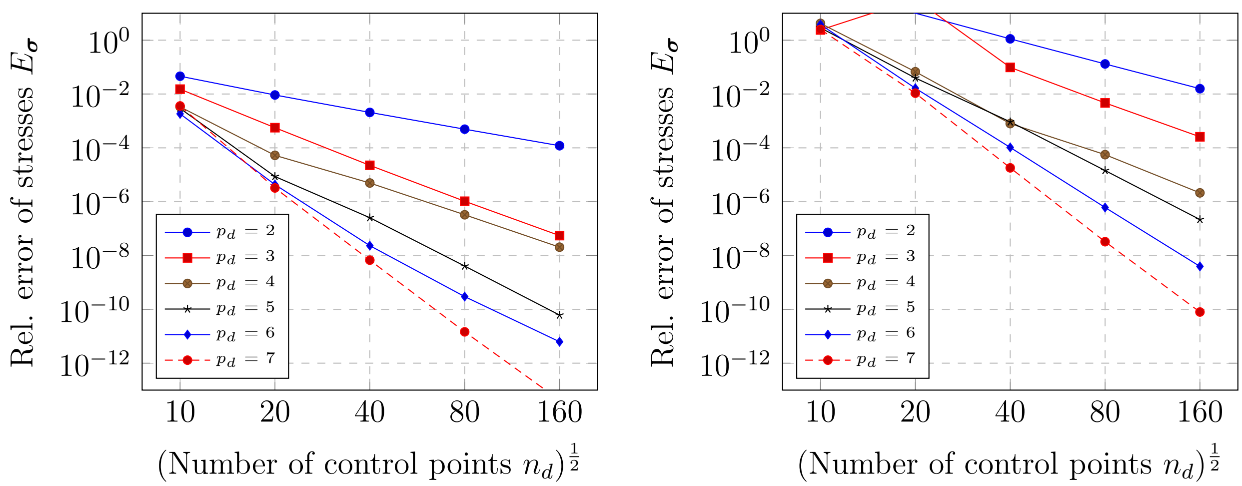

(a) Compressible ($\lambda = 1$)

(b) Nearly incompressible ($\lambda = 10^4$)

Figure A.2: Pressurized thick-walled cylinder: Relative error of stresses $E_{\boldsymbol{\sigma}}$, equal degree approximation ($p_s = p_d$), without hybrid approach.

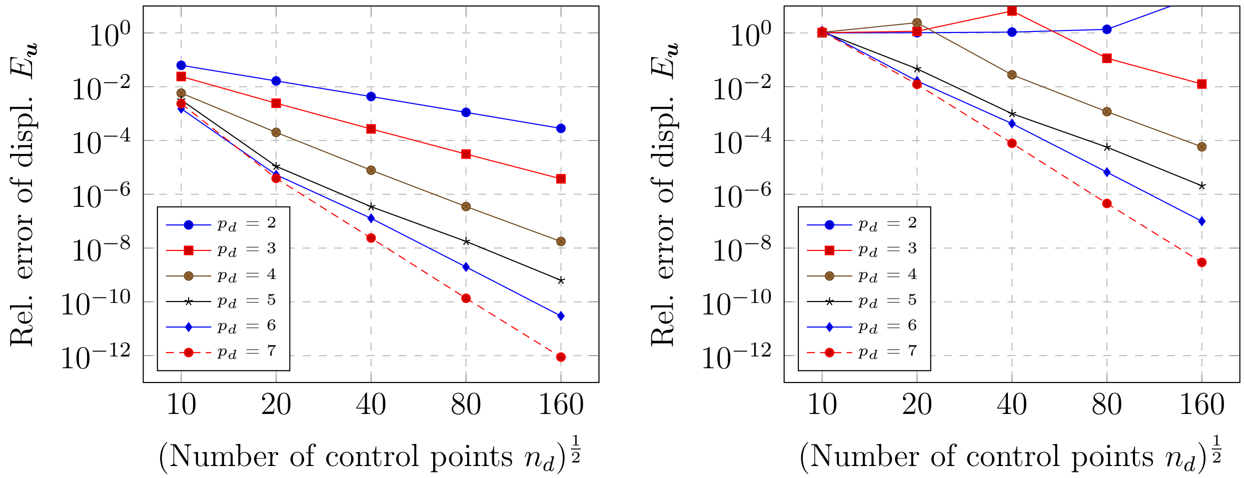

(a) Compressible ($\lambda = 1$)

(b) Nearly incompressible ($\lambda = 10^4$)

Figure A.3: Pressurized thick-walled cylinder: Relative error of displacements $E_{\boldsymbol{u}}$, enriched stress field ($p_s = p_d + 1$, same Bézier mesh), without hybrid approach.

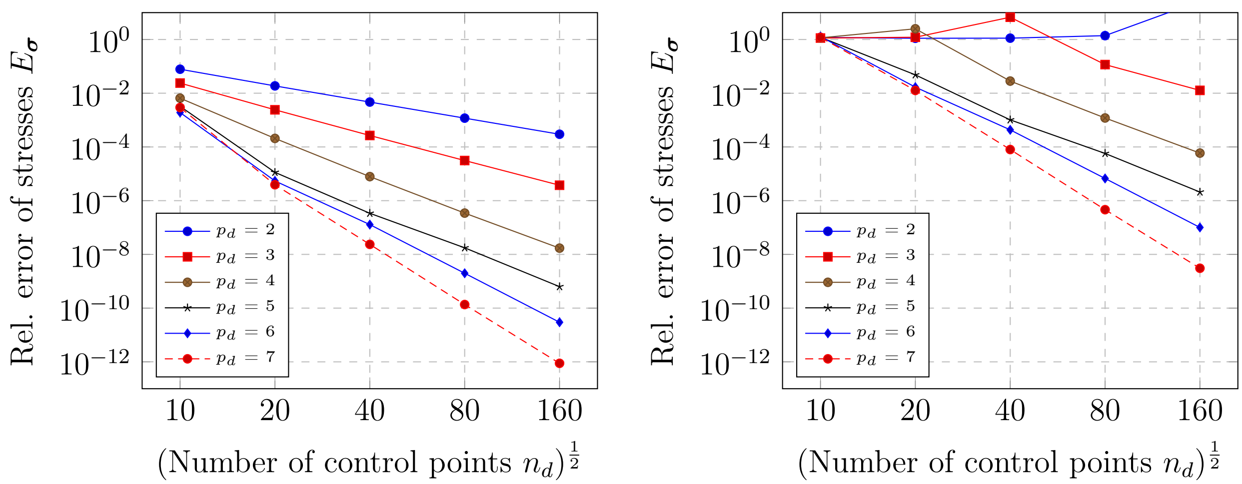

(a) Compressible ($\lambda = 1$)

(b) Nearly incompressible ($\lambda = 10^4$)

Figure A.4: Pressurized thick-walled cylinder: Relative error of stresses $E_{\boldsymbol{\sigma}}$, enriched stress field ($p_s = p_d + 1$, same Bézier mesh), without hybrid approach.

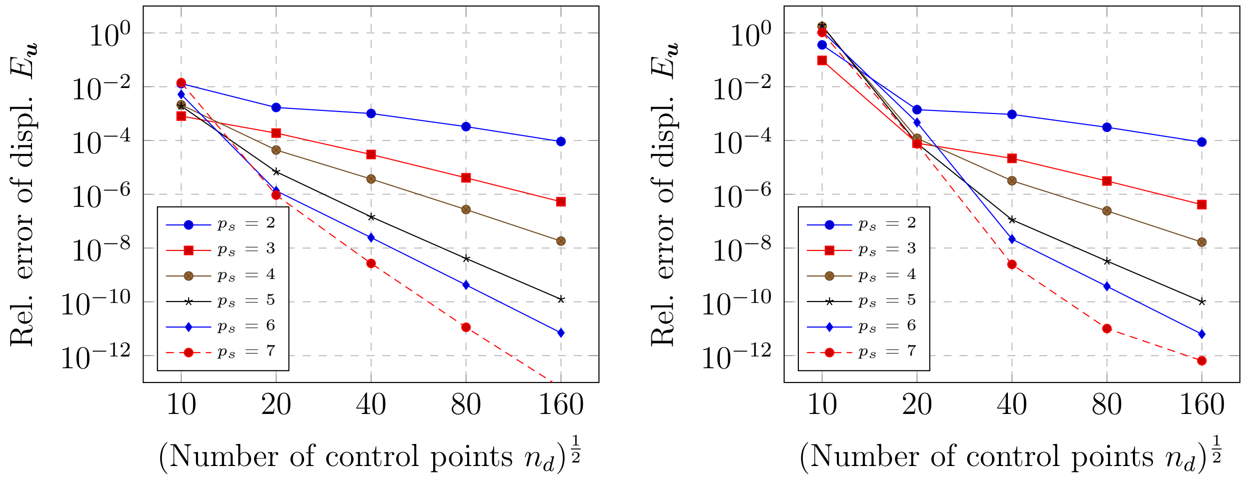

(a) Compressible ($\lambda = 1$) (b) Nearly incompressible ($\lambda = 10^4$)

Figure A.5: Pressurized thick-walled cylinder: Relative error of displacements $E_{\boldsymbol{u}}$, enriched displacement field ($p_d = p_s + 1$, same number of control points), without hybrid approach.

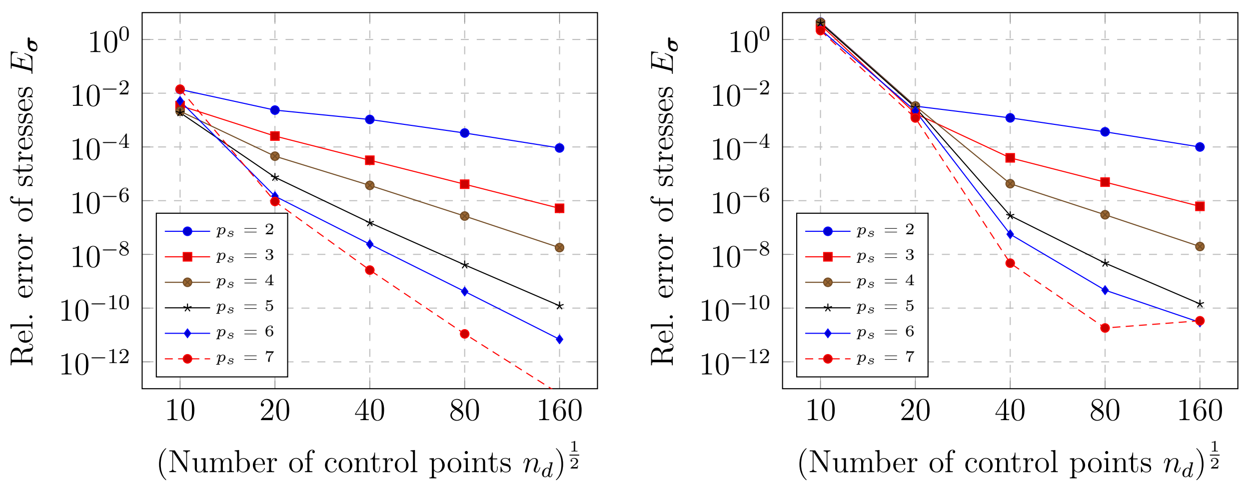

(a) Compressible ($\lambda = 1$) (b) Nearly incompressible ($\lambda = 10^4$)

Figure A.6: Pressurized thick-walled cylinder: Relative error of stresses $E_{\boldsymbol{\sigma}}$, enriched displacement field ($p_d = p_s + 1$, same number of control points), without hybrid approach.

Appendix A.2. Additional error plots for Cook's membrane (without hybrid approach)

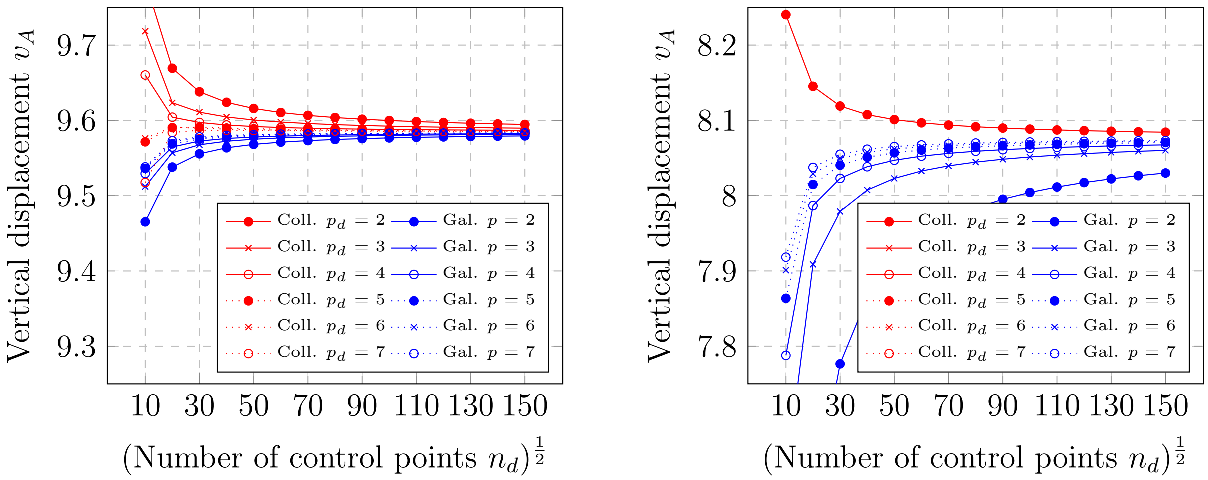

(a) Compressible ($\nu = 0.3$) (b) Nearly incompressible ($\nu = 0.4999$)

Figure A.7: Cook's membrane: Vertical displacement of top right corner (point A), equal degree approximation ($p_s = p_d$), without hybrid approach.

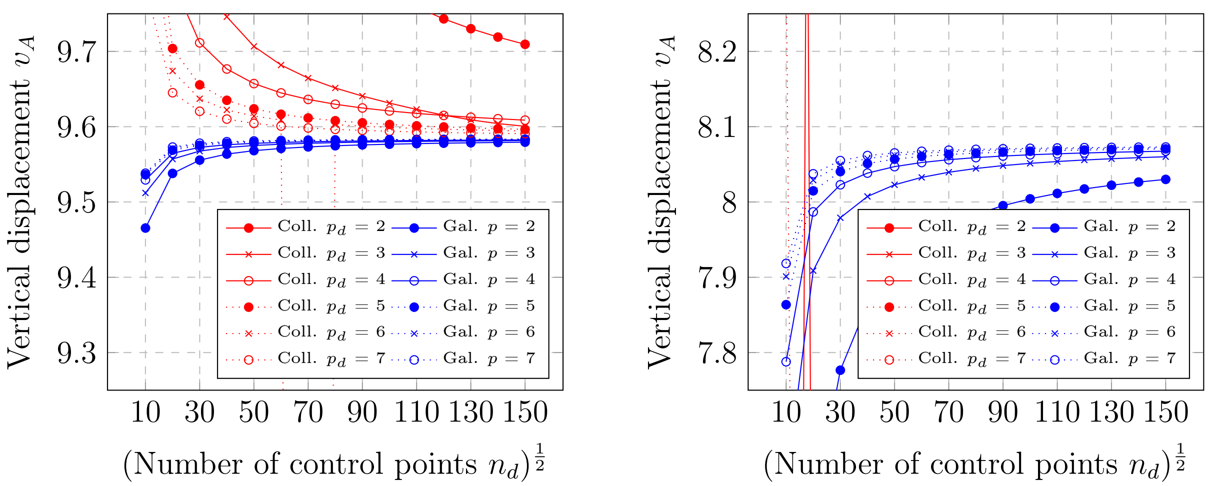

(a) Compressible ($\nu = 0.3$) (b) Nearly incompressible ($\nu = 0.4999$)

Figure A.8: Cook's membrane: Vertical displacement of top right corner (point A), enriched stress field ($p_s = p_d + 1$, same Bézier mesh), without hybrid approach.

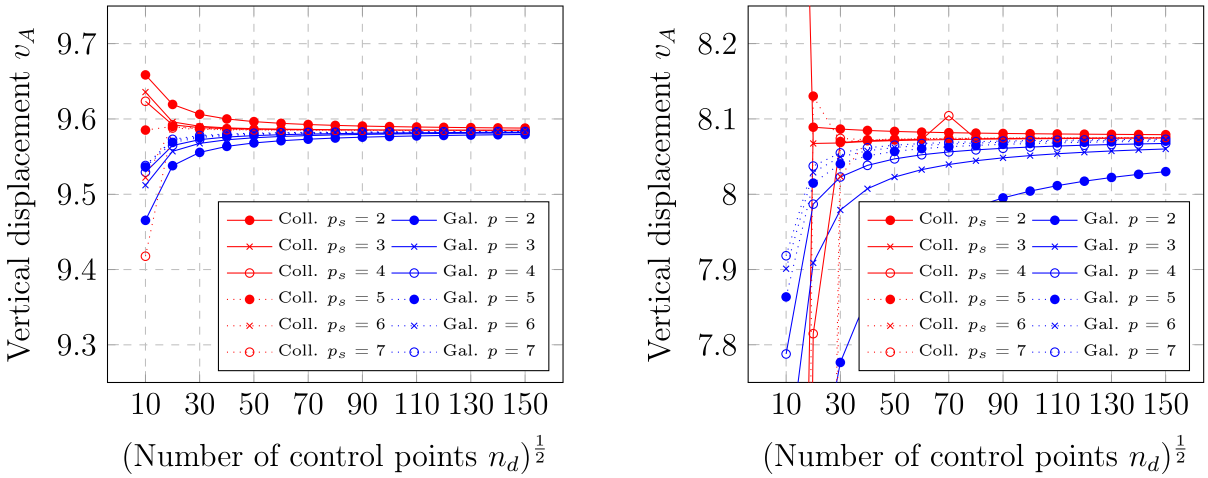

(a) Compressible ($\nu = 0.3$)

(b) Nearly incompressible ($\nu = 0.4999$)

Figure A.9: Cook's membrane: Vertical displacement of top right corner (point A), enriched displacement field ($p_d = p_s + 1$, same number of control points), without hybrid approach.

Appendix A.3. Stress plots for Cook's membrane

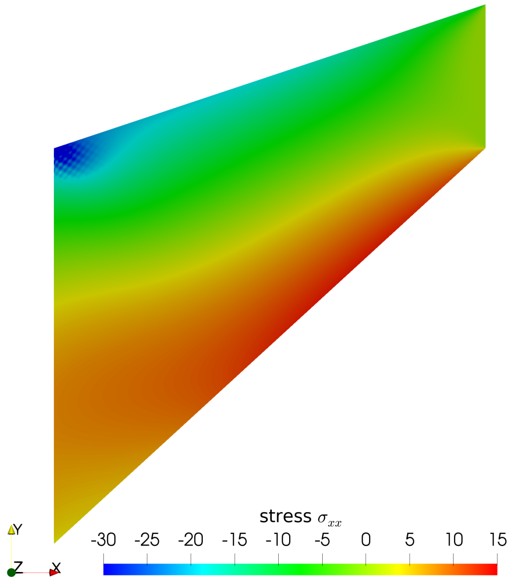

(a) Mixed Collocation ($p_d = 3, p_s = 2$)

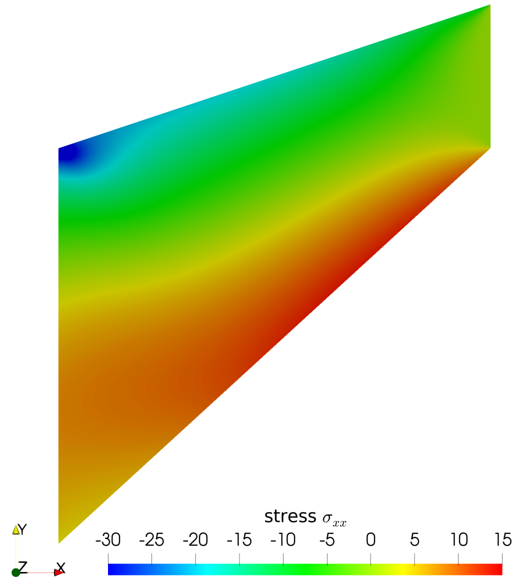

(b) Galerkin ($p = 2$)

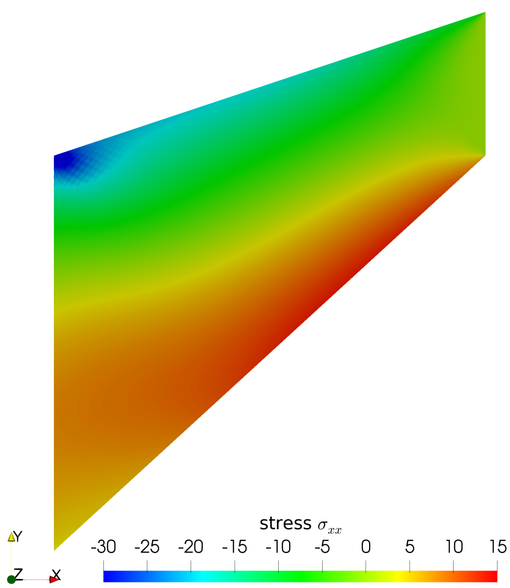

(c) Mixed Collocation ($p_d = 8, p_s = 7$)

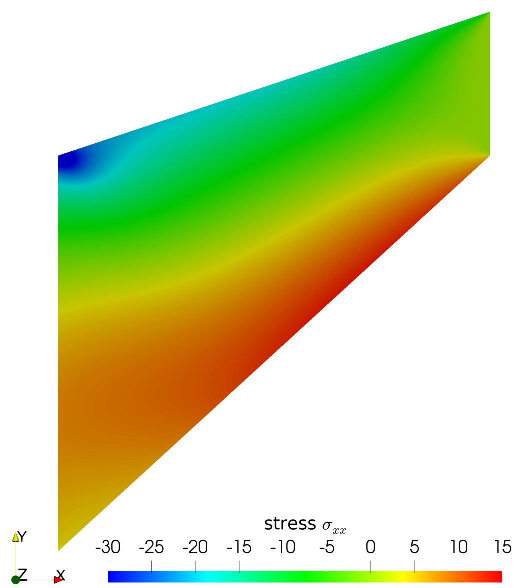

(d) Galerkin ($p = 7$)

Figure A.10: Cook's membrane: Stress σ_{xx}, compressible ($\nu = 0.3$).

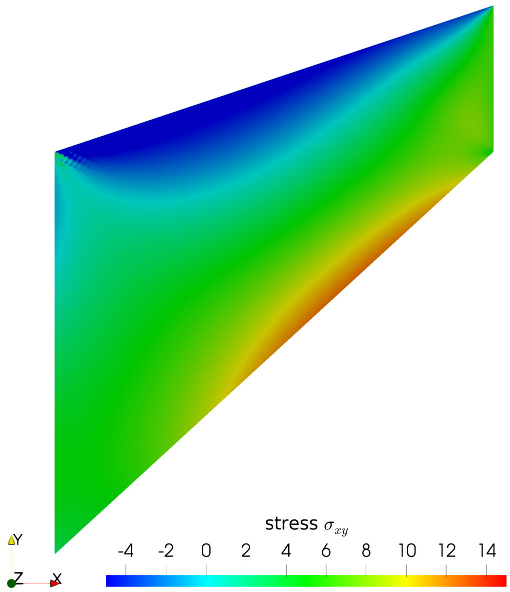

(a) Mixed Collocation ($p_d = 3, p_s = 2$)

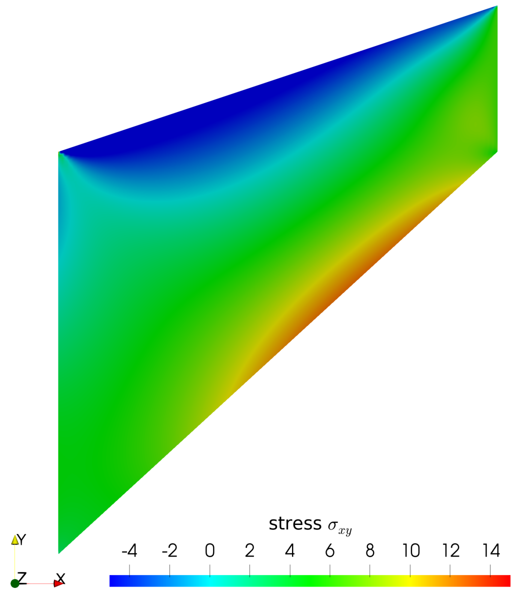

(b) Galerkin ($p = 2$)

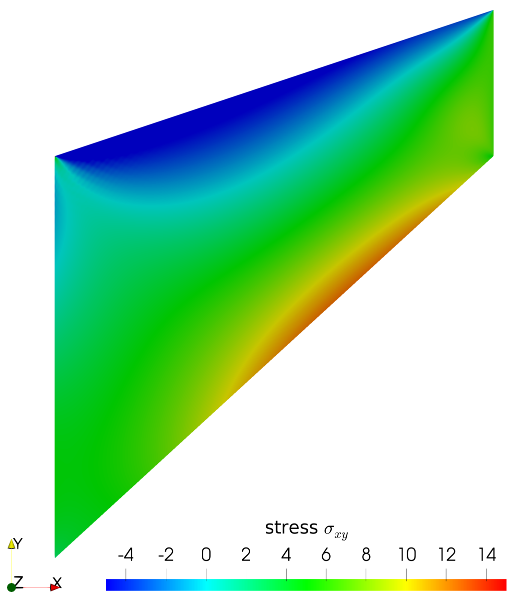

(c) Mixed Collocation ($p_d = 8, p_s = 7$)

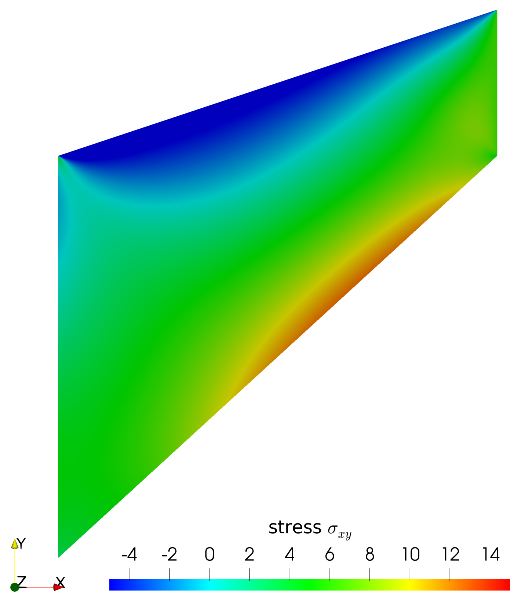

(d) Galerkin ($p = 7$)

Figure A.11: Cook's membrane: Stress σ_{xy}, compressible ($\nu = 0.3$).

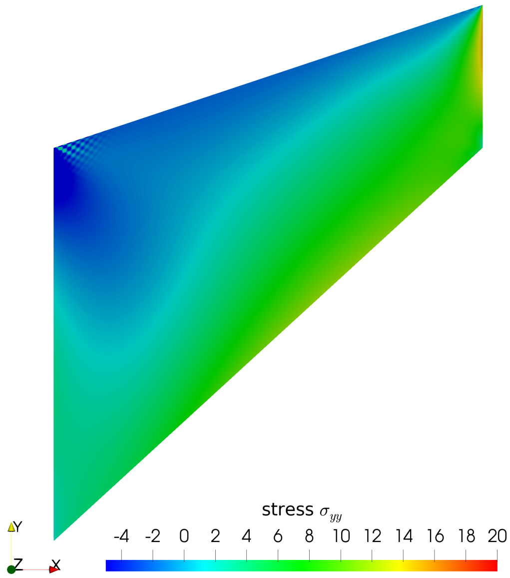

(a) Mixed Collocation ($p_d = 3, p_s = 2$)

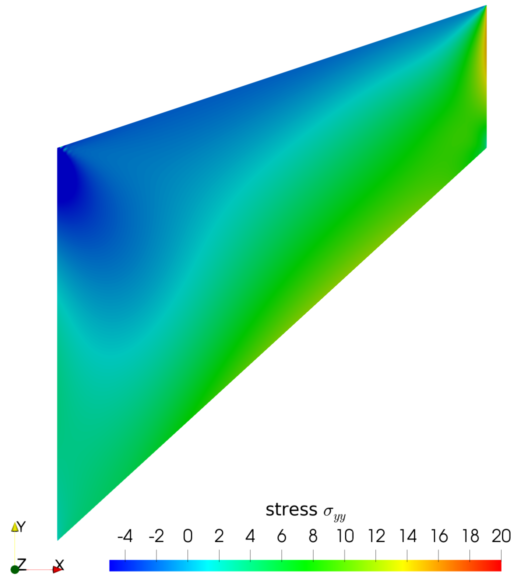

(b) Galerkin ($p = 2$)

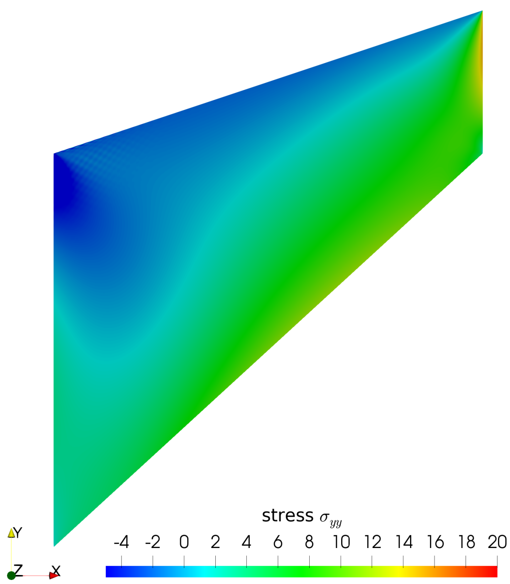

(c) Mixed Collocation ($p_d = 8, p_s = 7$)

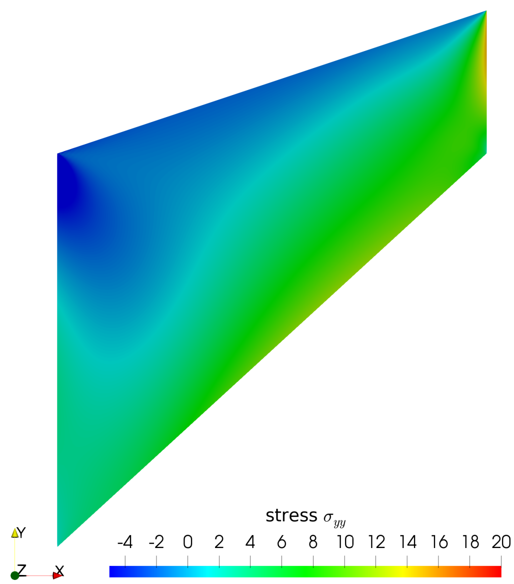

(d) Galerkin ($p = 7$)

Figure A.12: Cook's membrane: Stress σ_{yy}, compressible ($\nu = 0.3$).

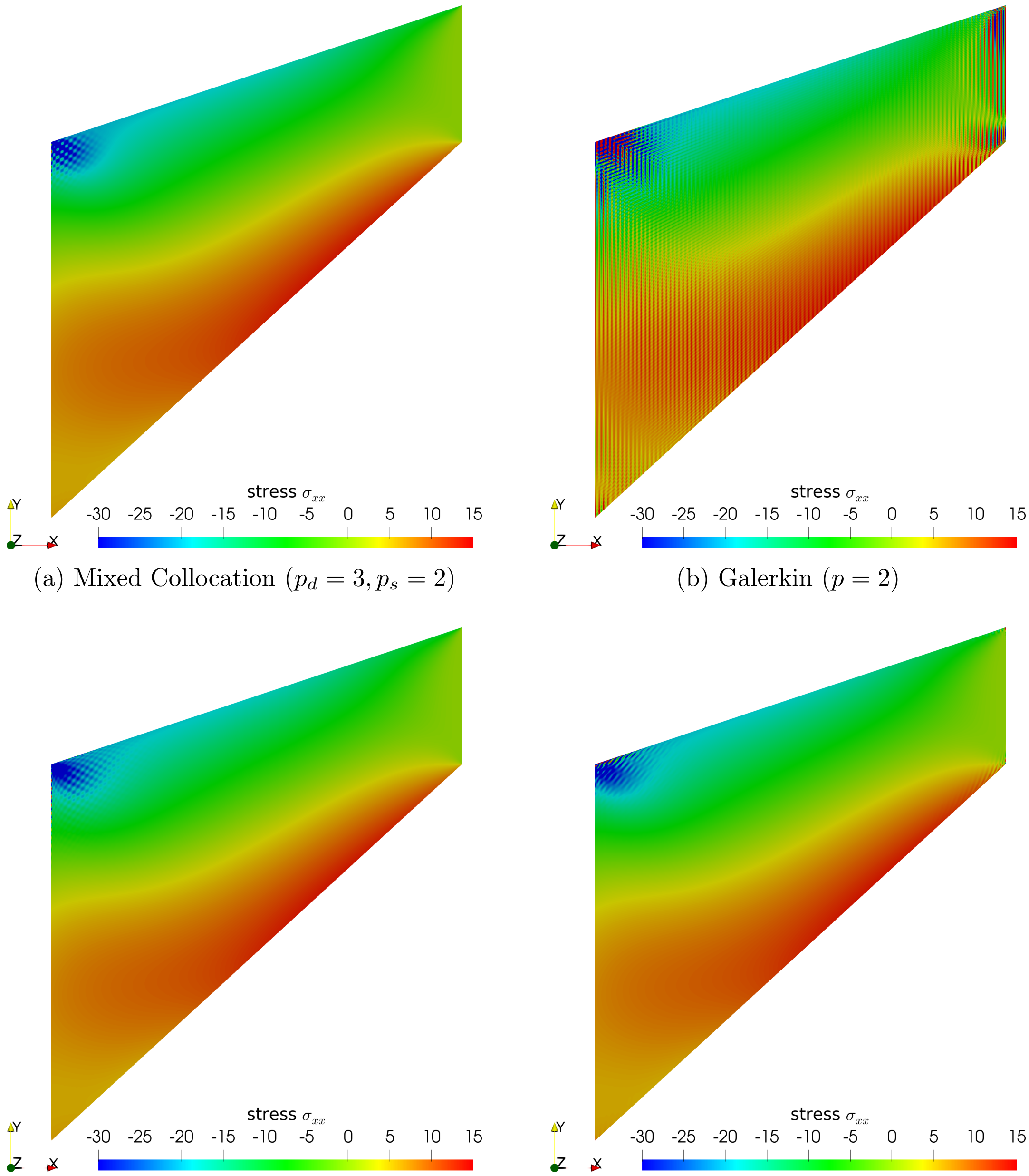

(a) Mixed Collocation ($p_d = 3, p_s = 2$)

(b) Galerkin ($p = 2$)

(c) Mixed Collocation ($p_d = 8, p_s = 7$)

(d) Galerkin ($p = 7$)

Figure A.13: Cook's membrane: Stress σ_{xx}, nearly incompressible ($\nu = 0.4999$).

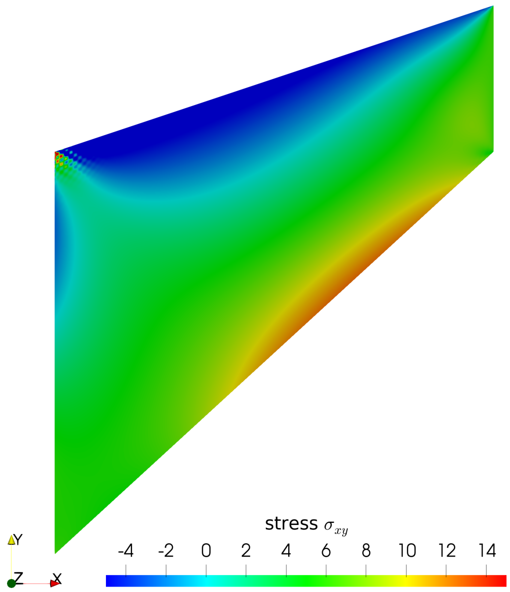

(a) Mixed Collocation ($p_d = 3, p_s = 2$)

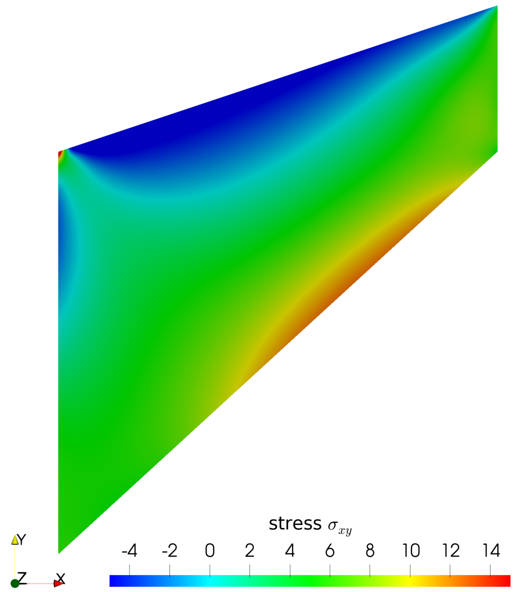

(b) Galerkin ($p = 2$)

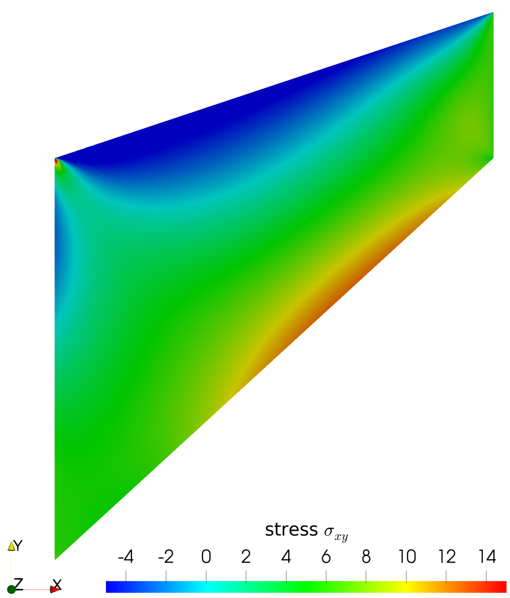

(c) Mixed Collocation ($p_d = 8, p_s = 7$)

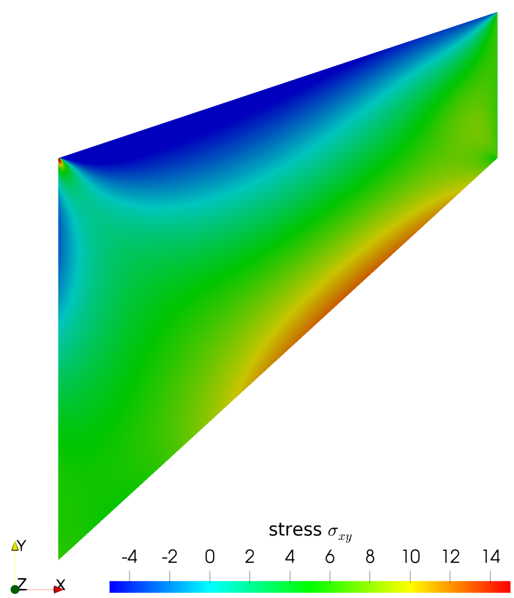

(d) Galerkin ($p = 7$)

Figure A.14: Cook's membrane: Stress σ_{xy}, nearly incompressible ($\nu = 0.4999$).

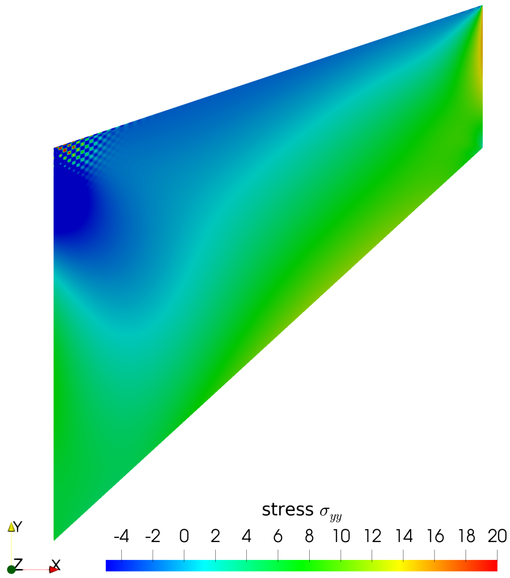

(a) Mixed Collocation ($p_d = 3, p_s = 2$)

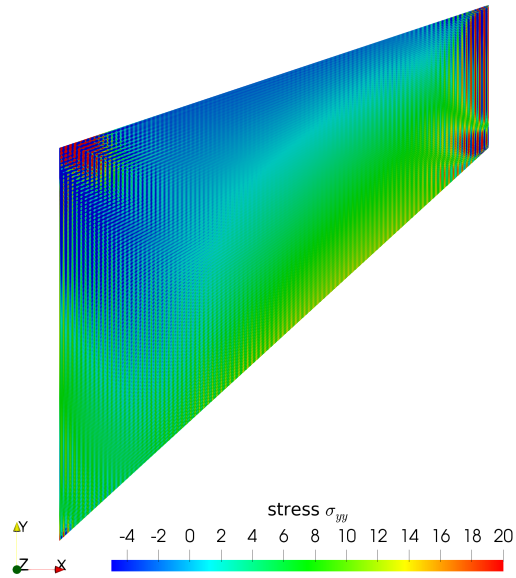

(b) Galerkin ($p = 2$)

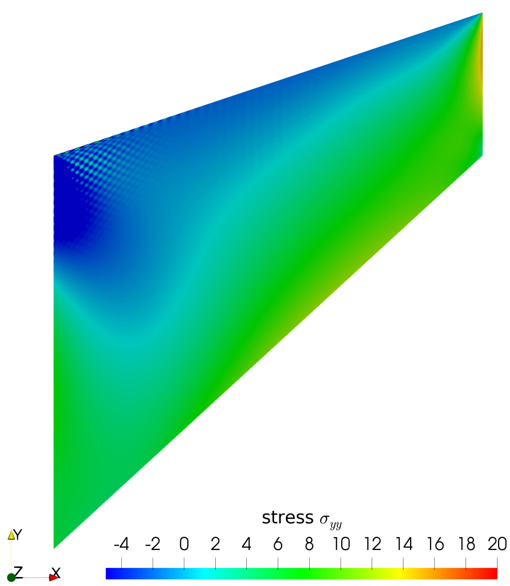

(c) Mixed Collocation ($p_d = 8, p_s = 7$)

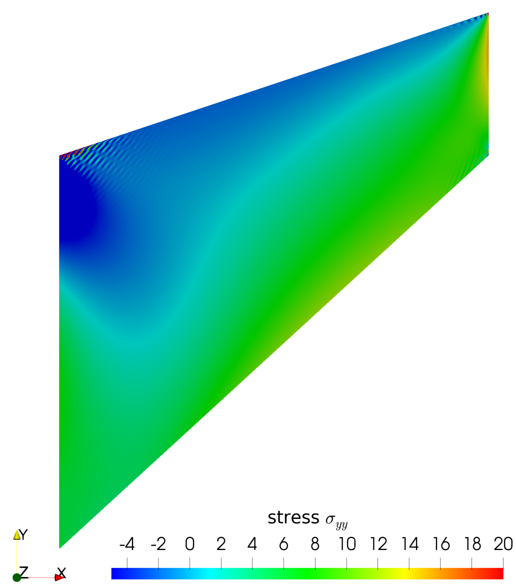

(d) Galerkin ($p = 7$)

Figure A.15: Cook's membrane: Stress σ_{yy}, nearly incompressible ($\nu = 0.4999$).

Appendix A.4. Equivalent plastic strain plots for quarter of annulus

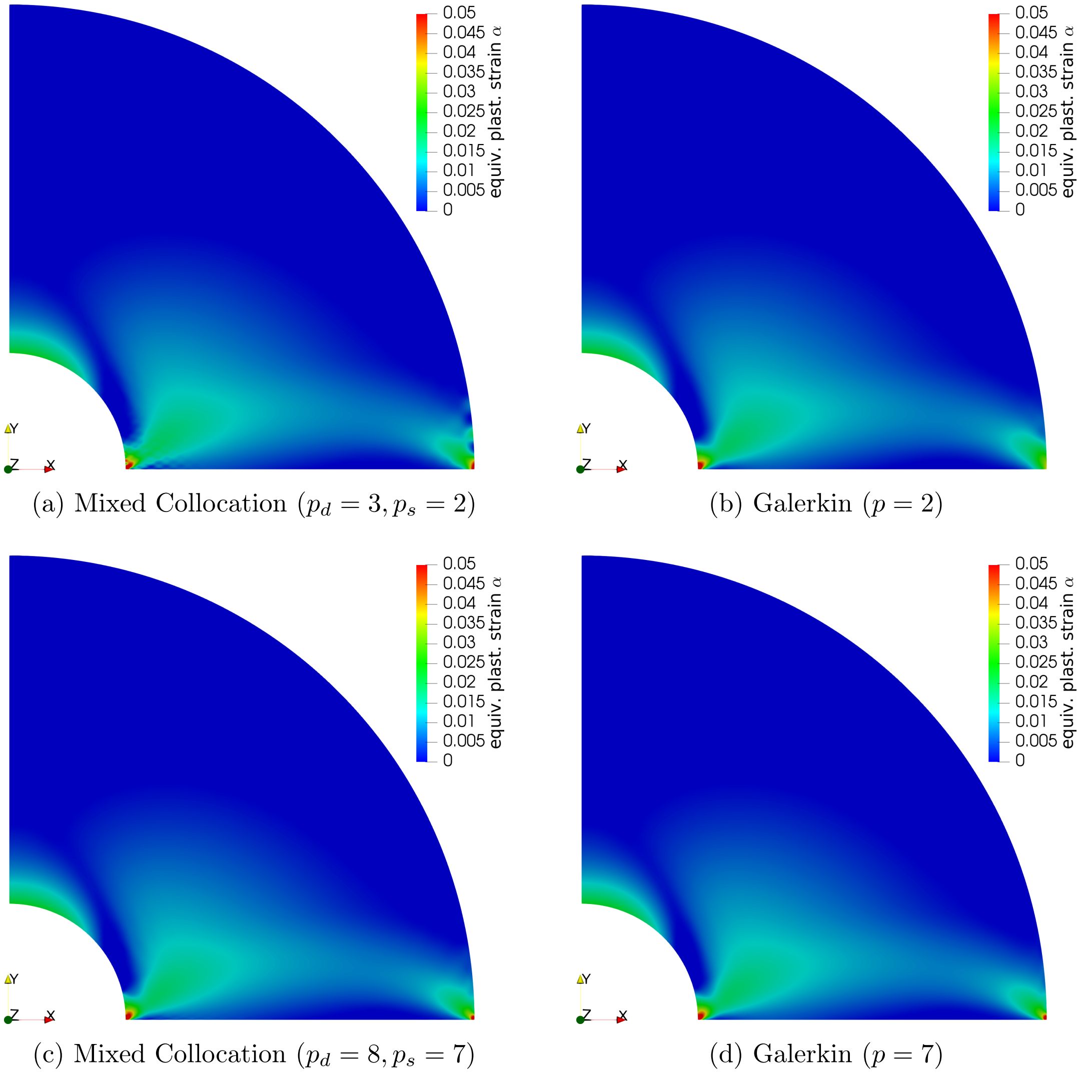

(a) Mixed Collocation ($p_d = 3, p_s = 2$)

(b) Galerkin ($p = 2$)

(c) Mixed Collocation ($p_d = 8, p_s = 7$)

(d) Galerkin ($p = 7$)

Figure A.16: Quarter of annulus: Equivalent plastic strain α, load step 20.

Appendix A.5. Equivalent plastic strain plots for clamped tensile test

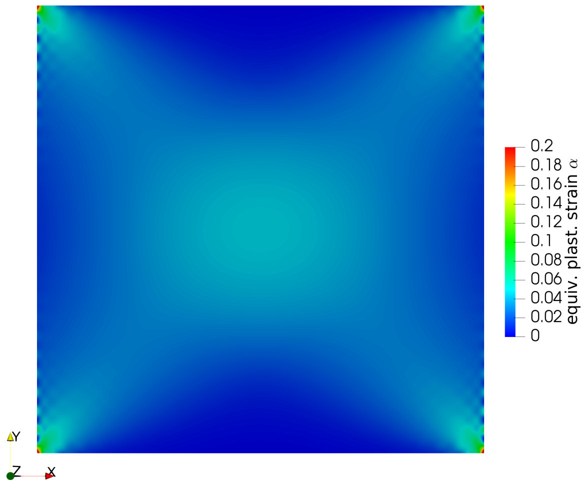

(a) Mixed Collocation ($p_d = 3, p_s = 2$)

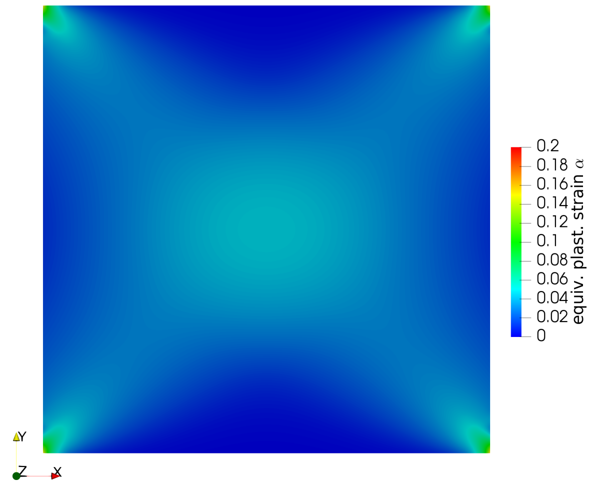

(b) Galerkin ($p = 2$)

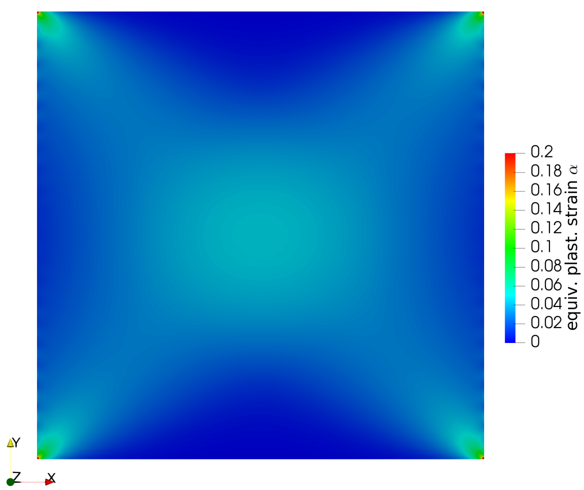

(c) Mixed Collocation ($p_d = 8, p_s = 7$)

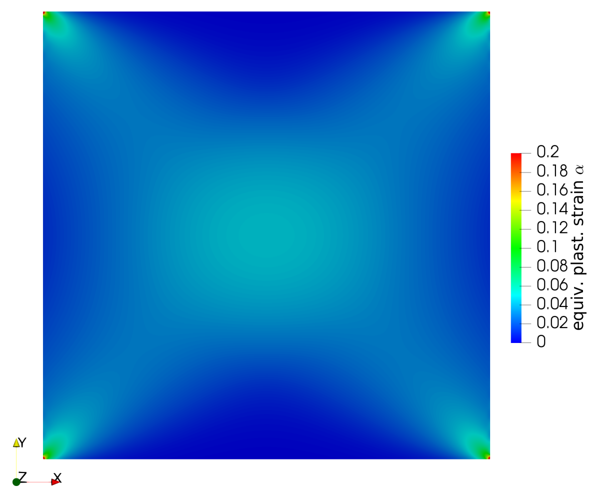

(d) Galerkin ($p = 7$)

Figure A.17: Clamped tensile test: Equivalent plastic strain α, load step 20.

Appendix A.6. Equivalent plastic strain and stress plots for plate with circular hole

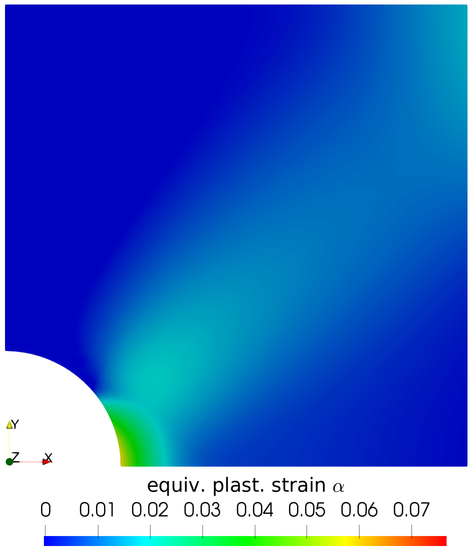

(a) Mixed Collocation ($p_d = 3, p_s = 2$)

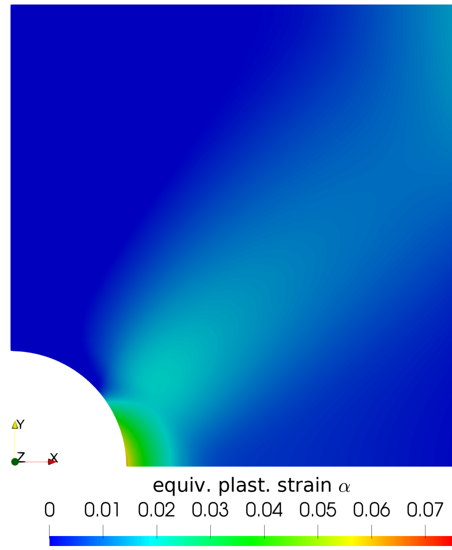

(b) Galerkin ($p = 2$)

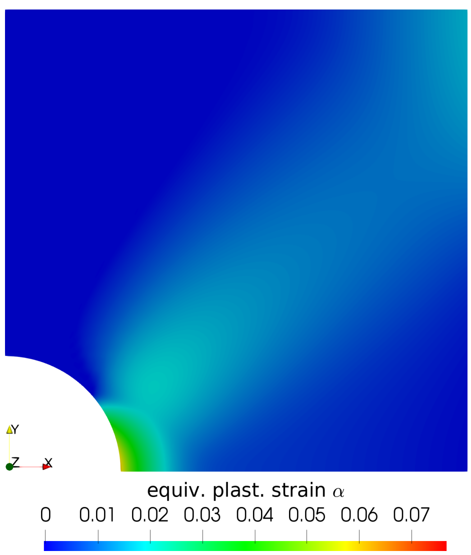

(c) Mixed Collocation ($p_d = 8, p_s = 7$)

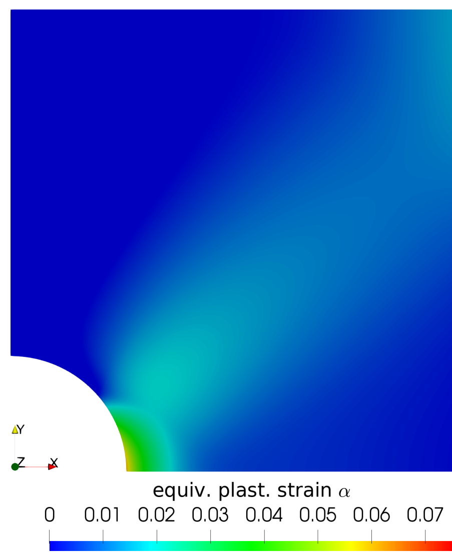

(d) Galerkin ($p = 7$)

Figure A.18: Plate with circular hole: Equivalent plastic strain α, load step 20.

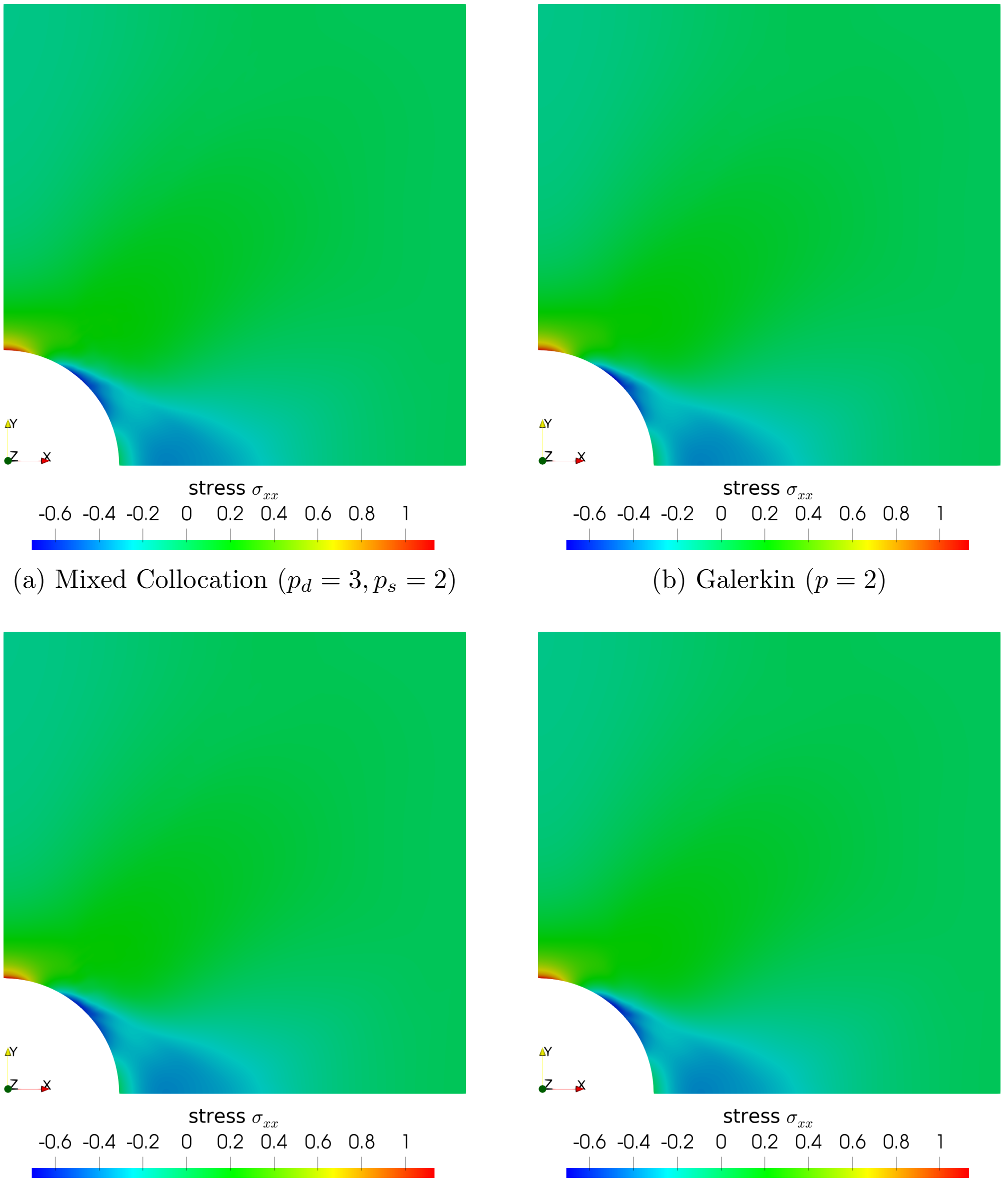

(a) Mixed Collocation ($p_d = 3, p_s = 2$)

(b) Galerkin ($p = 2$)

(c) Mixed Collocation ($p_d = 8, p_s = 7$)

(d) Galerkin ($p = 7$)

Figure A.19: Plate with circular hole: Stress σ_{xx}, load step 40.

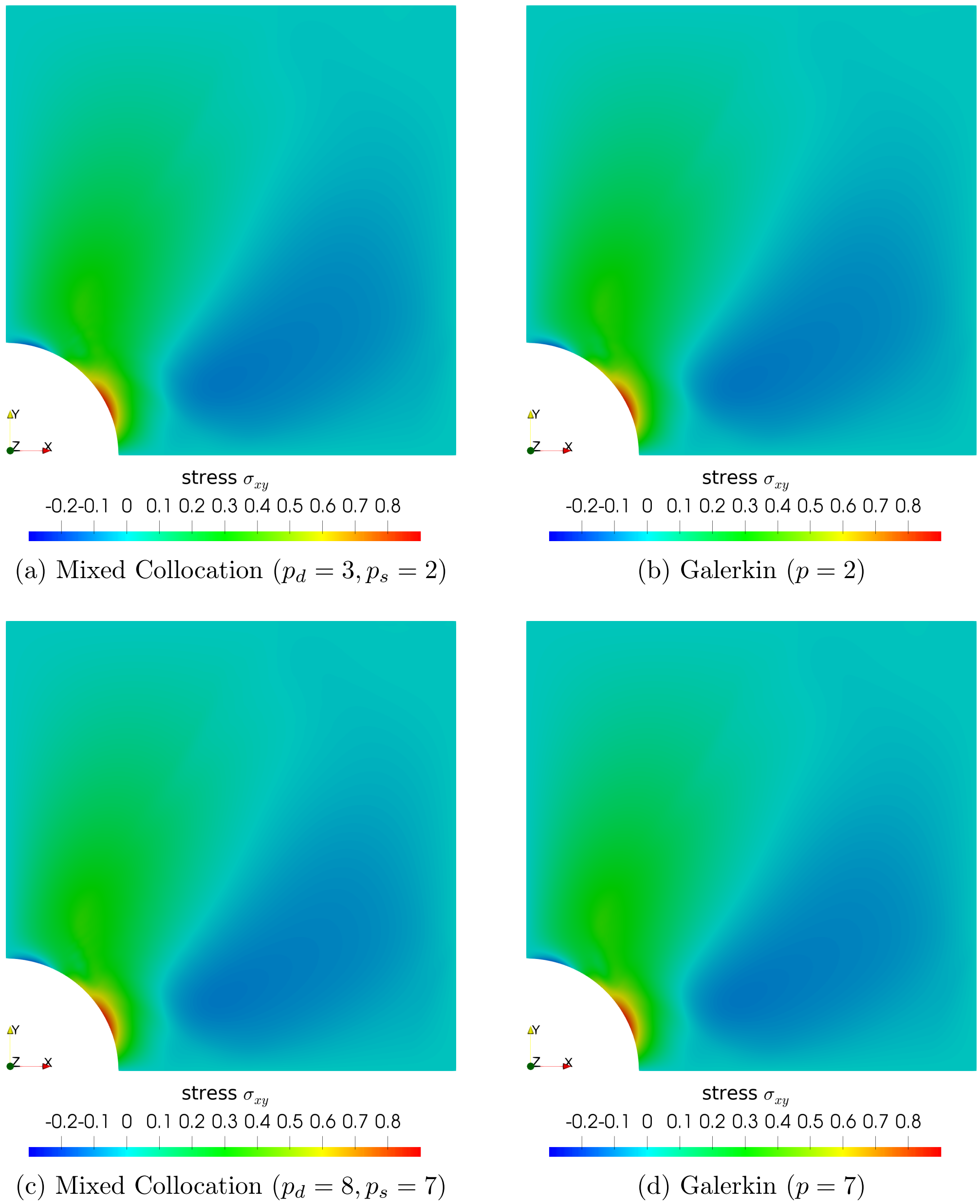

(a) Mixed Collocation ($p_d = 3, p_s = 2$)

(b) Galerkin ($p = 2$)

(c) Mixed Collocation ($p_d = 8, p_s = 7$)

(d) Galerkin ($p = 7$)

Figure A.20: Plate with circular hole: Stress σ_{xy}, load step 40.

(a) Mixed Collocation ($p_d = 3, p_s = 2$)

(b) Galerkin ($p = 2$)

(c) Mixed Collocation ($p_d = 8, p_s = 7$)

(d) Galerkin ($p = 7$)

Figure A.21: Plate with circular hole: Stress σ_{yy}, load step 40.